



MÁSTER EN INGENIERÍA INDUSTRIAL

TRABAJO FIN DE MASTER

RECONSTRUCTION OF PLANAR FUEL CONCENTRATION MEASUREMENTS IN A DIESEL SPRAY FROM LINE-OF-SIGHT DIFFUSE BACK ILLUMINATION IMAGING.

Autor: Carlos de la Cámara Castillo

Director: Caroline Genzale

Madrid

Declaro, bajo mi responsabilidad, que el Proyecto presentado con el título
Reconstruction of planar fuel concentration measurements in a diesel spray
from line-of-sight diffuse back illumination imaging.

en la ETS de Ingeniería - ICAI de la Universidad Pontificia Comillas en el
curso académico 2020-2021 es de mi autoría, original e inédito y
no ha sido presentado con anterioridad a otros efectos. El Proyecto no es plagio
de otro, ni total ni parcialmente y la información que ha sido tomada
de otros documentos está debidamente referenciada.

Fdo.: Carlos de la Camara Castillo

Fecha: 07/12/2020



Autorizada la entrega del proyecto

EL DIRECTOR DEL PROYECTO

Fdo.: Caroline Genzale

Fecha: 07/18/2020



12/18/20



MÁSTER EN INGENIERÍA INDUSTRIAL

TRABAJO FIN DE MASTER

RECONSTRUCTION OF PLANAR FUEL CONCENTRATION MEASUREMENTS IN A DIESEL SPRAY FROM LINE-OF-SIGHT DIFFUSE BACK ILLUMINATION IMAGING.

Autor: Carlos de la Cámara Castillo

Director: Caroline Genzale

Madrid

Acknowledgements

This year has been a unique and challenging one for all of us, that is why I want to thank all the people that have supported me. First of all, I want to thank my advisor Caroline, who gave me the chance to work in this great research group. I appreciate all the advice she has given me since the very beginning. This thesis also gave me the opportunity to meet two wonderful people: Ken and Conner. Ken's guidance was very valuable for my onboarding at the lab and Conner has been not only an extraordinarily helpful figure at the lab but also a great friend.

Second, this journey would have been impossible without my family. My mom, father, and brother have been an unlimited source of motivation and affection. I really want to thank them not only for the support during this tough year but also throughout my life. I hope that someday I can repay them for all the effort and sacrifices they have done for me.

I also want to show my appreciation to Jose and Alvaro. The three of us have faced many problems but working together through these challenges has definitely made our friendship stronger. I want to thank them for their fellowship and help throughout this incredible journey.

Finally, let me thank my second family: Mike and Cristian. It has been such a rewarding experience to live with them. I greatly appreciate their company in the good times and the bad. I have learned so many things from them and built an extraordinarily strong relationship that I hope to keep developing for many more years.

RECONSTRUCTION OF PLANAR FUEL CONCENTRATION MEASUREMENTS IN A DIESEL SPRAY FROM LINE-OF-SIGHT DIFFUSE BACK ILLUMINATION IMAGING.

Autor: de la Cámara Castillo, Carlos.

Director: Genzale, Caroline.

Entidad Colaboradora: Georgia Institute of Technology

RESUMEN DEL PROYECTO

Este proyecto trata de validar los datos de un nuevo método de línea de visión de captura de imágenes de un spray diésel. Los datos medidos se compararon con mediciones planares de dispersión de Rayleigh, mediante la transformada inversa de Abel. Se obtuvo una buena validación de los datos, a falta de comprobar una dependencia de cierto parámetro con respecto a la presión.

Palabras clave: Spray diésel, concentración de combustible, mediciones planares, mediciones de línea de visión, reconstrucción, transformada inversa de Abel, UV-Vis DBI

1. Introducción

Hoy en día, el cambio climático y la contaminación están muy presentes en la sociedad, y la preocupación por ellos va en aumento. Respecto a las emisiones, el CO₂ es un gas muy significativo para el efecto invernadero y que se usa como referencia para medir el impacto de otros gases. El 24% de las emisiones globales de CO₂ son emitidas por el sector de transporte [1], en el cual los motores diésel tienen un gran papel. Los motores diésel emiten entre un 11% y un 40% menos de CO₂; esto sumado a otras ventajas como un menor consumo, hacen este tipo de motores muy atractivos. Sin embargo, emiten mayores cantidades de partículas y óxidos de nitrógeno. Es por ello, por lo que gran parte de la investigación está enfocada a reducir este tipo de emisiones en los motores diésel, mediante una mayor comprensión de la combustión.

Muchos proyectos de investigación han mostrado la estrecha relación que hay entre las emisiones y la mezcla aire-combustible. Para ello, se han desarrollado diferentes técnicas de captura de imágenes de la inyección del spray en una cámara de combustible. Entre ellas podemos diferenciar dos grandes tipos: mediciones planares y mediciones de línea de visión.

Con las mediciones planares se pueden obtener datos de la concentración de combustible sobre un plano del spray. Un ejemplo de esta técnica es la dispersión de Rayleigh. Con este método se han obtenido datos no solo cualitativos sino cuantitativos de la concentración de combustible. Es por ello por lo que es una gran base de comparación y validación de otras técnicas.

Por otro lado, las imágenes capturadas con técnicas de línea de visión proporcionan datos de intensidad proporcional a la trayectoria que atraviesa la luz emitida. Con ello, luego se pueden obtener mapas de concentración proyectada de combustible.

En el grupo de laboratorio de este proyecto se está desarrollando una nueva técnica de línea de visión que necesita ser validada.

2. Definición del proyecto

Este Proyecto nace con el objetivo de desarrollar una metodología para validar los datos obtenidos con la nueva técnica de línea de visión en desarrollo, su nombre es retroiluminación difusa por luz visible y ultravioleta (cuyas siglas en inglés son UV-Vis DBI). La metodología empleada consiste en utilizar la transformada inversa de Abel para convertir los datos de concentración proyectada de combustible en concentración planar de combustible. Además, dado que este tipo de experimentos suelen estar limitados en cuanto al número de inyecciones disponibles para obtener datos por el elevado coste económico y de tiempo que suponen, se hará un análisis para comprobar cuantas inyecciones son necesarias para obtener una media representativa del espray.

3. Descripción del modelo/sistema/herramienta

El Sistema empleado en el laboratorio consiste en una cámara de combustión de presión constante y flujo continuo. En ella se recrean las condiciones dictadas por el Spray A de ECN (Engine Combustion Network). Las principales condiciones de la cámara de combustión son:

- Temperatura: 900K
- Presión: 60 bar
- Gas: nitrógeno
- Combustible: 99.25% concentración molar de dodecano y 0.75% de concentración molar de naftaleno
- Duración de la inyección electrónica: 3ms

Por otro lado, se encuentra el sistema óptico que se encarga de capturar las imágenes. Para ello se emplea un láser que es capaz de generar simultáneamente dos longitudes de onda: 280nm (luz ultravioleta) y 560nm (luz visible). Ambas longitudes de onda atraviesan el espray diésel de la cámara de combustión. Al otro lado de la cámara de combustión, la luz ultravioleta y visible son separadas y capturadas por dos cámaras de alta velocidad.

Dado que la luz visible es únicamente dispersada por la región de líquido del espray, esta técnica permite diferenciar la región de líquido de la de vapor. Las imágenes capturadas son procesadas y ajustadas para eliminar efectos no deseado originados por otras causas diferentes al espray.

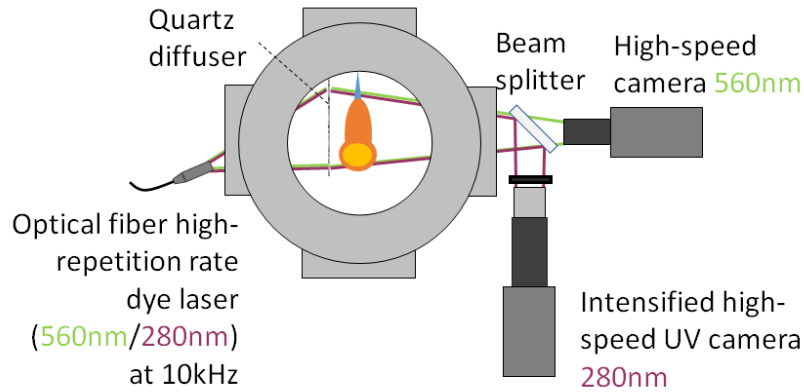


Ilustración 1. Esquema de la cámara de combustión y equipo óptico. [2]

Después, siguiendo la ley de Beer-Lambert se puede calcular la profundidad óptica de las imágenes, que se utiliza para calcular la concentración proyectada de combustible posteriormente.

Para el comprobar el número de inyecciones necesarias para obtener una media representativa del spray, se analizaron varios aspectos. En primer lugar, una vez se había ajustado la escala temporal del spray y eliminado los valores atípicos, se procedió a analizar la desviación estándar. Con ello, se comprueba cuantas inyecciones son necesarias para capturas las fluctuaciones del spray. Después, se estudió el intervalo de confianza con respecto al número de muestras/inyecciones usadas. Con estos dos análisis se pudo llegar a una conclusión respecto al número de muestras/inyecciones necesarias.

Una vez obtenida la concentración media proyectada de combustible se pasa a emplear la transformación inversa de Abel. Esta transformada relaciona la concentración radial de una función con su función de línea de visión, se puede observar más claramente en Ecuación 1 e Ilustración 2.

$$f(r) = -\frac{1}{\pi} \int_r^{\infty} \frac{dF(y)}{dy} \frac{1}{\sqrt{y^2 - r^2}} dy \quad \text{Ecuación 1}$$

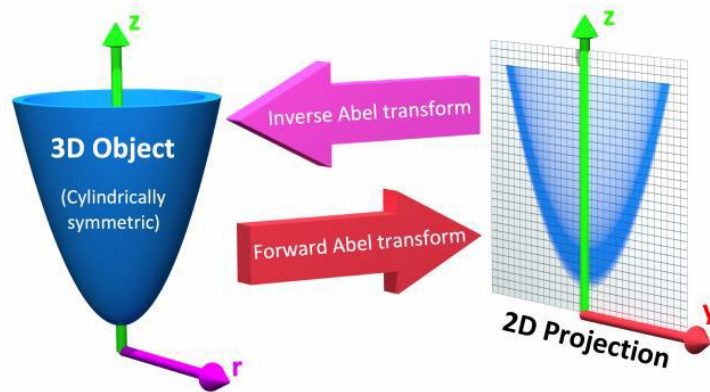


Ilustración 2. Esquema de la transformada de Abel. [3]

Previo a aplicar la transformada en nuestros datos, se analizó su comportamiento con varias ecuaciones analíticas, además de con otros datos experimentales proporcionados por ECN. Con lo aprendido al realizar este análisis previo, se aplicó la transformada inversa de Abel a nuestros datos. Y finalmente se comprueban los resultados con los datos de concentración planar de dispersión de Rayleigh proporcionados por ECN.

4. Resultados

En primer lugar, respecto al número de muestras necesarias, se comprobó que la desviación estándar tendía a estabilizarse en torno a las 30-40 muestras. Por otro lado, el intervalo de confianza se reduce a un 5-6% del valor de la media. Evidentemente, si se añadan más muestras el intervalo de confianza será cada vez más pequeño, sin embargo, los grandes costes que supone cada muestra adicional hacen que este número se desee mantener lo más bajo posible. Por lo tanto, para este tipo de experimento se concluyó que 30-40 eran suficientes para capturar las fluctuaciones del spray, manteniendo a la vez un intervalo de confianza suficientemente bajo. En la ilustración a continuación se puede observar el intervalo de confianza calculado para diferentes números de muestras.

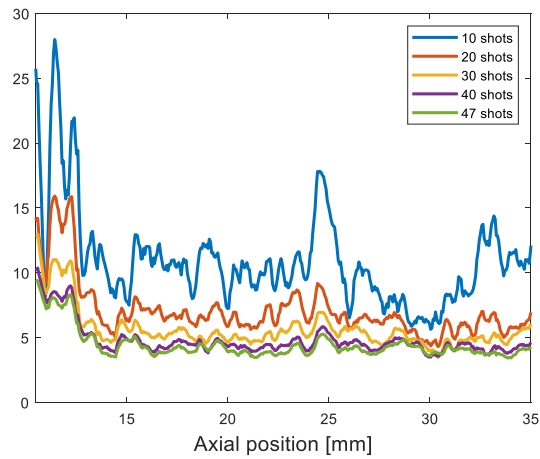


Ilustración 3. Intervalo de confianza (%), en la línea central del spray usando diferente número de muestras

Los resultados de la transformada inversa de Abel para obtener la concentración planar pueden observarse en la Ilustración 4. Lo primero que se observa es que la concentración calculada está por debajo de la concentración medida por ECN, en torno a un factor de dos. La hipótesis planteada por nuestro grupo sobre origen de este factor es la dependencia de presión de la naftalina. Este fenómeno se investigará en el trabajo futuro de grupo, sin embargo, para este trabajo se continúa aplicando un factor de corrección de dos.

Con ello, se observa como la tendencia de la concentración planar de combustible sobre la línea central del spray concuerda con los datos de dispersión de Rayleigh. Por otro lado, la concentración también concuerda en los gráficos axiales. Aunque en la figura solo se han representado cuatro posiciones axiales de la concentración planar, se comprobó que el resto de posiciones también concordaban los datos.

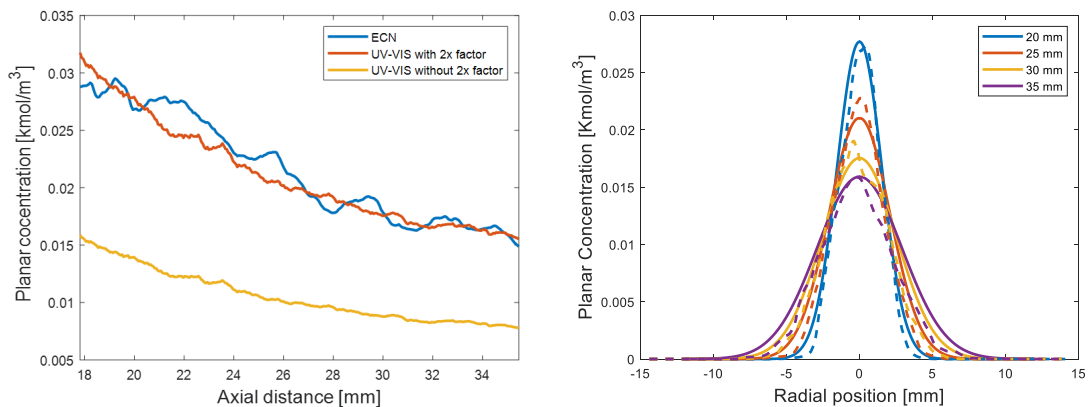


Ilustración 4. Validación de la concentración planar de combustible transformada respecto a la medida por ECN en la línea central del spray (izquierda) y en cuatro posiciones axiales (derecha).

5. Conclusiones

En primer lugar, se encontró que el número de muestras necesarias para obtener una media que represente las fluctuaciones del spray con un intervalo de confianza en torno al 5%, eran 30-40 inyecciones.

En segundo lugar, a falta de comprobar la dependencia de presión de la naftalina, se comprobó que la concentración planar de combustible transformada coincidía con la tendencia mostrada por los datos de ECN.

Finalmente se comprobó también que la incertidumbre introducida por la transformada inversa de Abel es baja cuando la resolución de la función es suficiente, tiende a cero y no tiene cambios bruscos en ella.

6. Referencias

- [1] I. E. Agency, "CO2 emissions from fuel combustion," 2019.
- [2] C. Godbold, F. Poursadegh, O. Bibik, C. de la Camara Castillo and C. Genzale, "A multi-wavelength extinction imaging diagnostic for quantifying diesel spray mixing at engine-relevant conditions," ASME, 2020.
- [3] D. Hickstein, S. Gibson, R. Yurchak, D. Das and M. Ryazanov, "A direct comparison of high-speed methods for the numerical Abel transform," Review of Scientific Instruments 90, 2019

RECONSTRUCTION OF PLANAR FUEL CONCENTRATION MEASUREMENTS IN A DIESEL SPRAY FROM LINE-OF-SIGHT DIFFUSE BACK ILLUMINATION IMAGING.

Author: de la Cámara Castillo, Carlos.

Supervisor: Genzale, Caroline.

Collaborating Entity: Georgia Institute of Technology

ABSTRACT

This project tries to validate the data from a new line-of-sight imaging method for a diesel spray. The measured data was compared with Rayleigh scattering planar measurements, using the inverse Abel transform. A good validation of the data was obtained; nevertheless, there is verification to be done in the future work about a pressure dependence of a parameter.

Keywords: Diesel spray, fuel concentration, planar measurements, line-of-sight, reconstruction, inverse Abel transform, UV-Vis DBI

1. Introduction

Nowadays, climate change and pollution are very present in society, and its concern for them is increasing. Regarding emissions, CO₂ is a very significant gas for the greenhouse effect and is used as a reference to measure the impact of other gases. 24% of global CO₂ emissions are emitted by the transport sector [1], in which diesel engines play a major role. Diesel engines emit between 11% and 40% less CO₂; this added to other advantages such as lower consumption, make this type of engine very attractive. However, they emit higher amounts of particulates and nitrogen oxides. That is why much of the research is focused on reducing this type of emissions in diesel engines through a better understanding of combustion.

Many research projects have shown the tied relation between emissions and the air-fuel mixture. Different techniques have been developed to capture images of the injection of the spray into a fuel chamber. Among them, we can differentiate two main types: planar measurements and line of sight measurements.

With planar measurements, planar fuel concentration data can be obtained. An example of this technique is Rayleigh scattering. With this method, not only qualitative but quantitative data of fuel concentration have been obtained. This is why it is an excellent basis for comparison and validation of other techniques.

On the other hand, images captured with line-of-sight techniques provide data of intensity proportional to the path that the emitted light passes through, then projected fuel concentration maps could then be obtained. A new line-of-sight technique is being developed in the laboratory group for this project that needs to be validated.

2. Project objectives

The objective of this project is to develop a methodology to validate the data obtained with the new line-of-sight technique; its name is Ultraviolet-Visible Diffuse Back-Illumination (UV-Vis DBI). The methodology used consists of using the inverse Abel transform to convert the projected fuel concentration data into planar fuel concentration.

In addition, since these types of experiments are usually limited in terms of the number of injections available to obtain data due to the high cost and time involved, an analysis will be carried out to verify how many injections are necessary to obtain a representative mean of the spray.

3. Model/system/ tool description

The system used in our laboratory consists of a constant pressure and continuous flow combustion vessel. The conditions dictated by Spray A from ECN (Engine Combustion Network) are recreated. The main conditions of the combustion chamber are:

- Temperature: 900K
- Pressure: 60 bar
- Gas: nitrogen
- Fuel: 99.25% molar concentration of dodecane and 0.75% molar concentration of naphthalene
- Commanded injection duration: 3ms

On the other hand, there is an optical setup that is responsible for capturing the images. A laser capable of simultaneously generating two wavelengths: 280nm (ultraviolet light) and 560nm (visible light) is used. Both wavelengths pass through the diesel spray from the combustion chamber. On the other side of the combustion chamber, the ultraviolet and visible light are separated and captured by two high-speed cameras.

Since visible light is only scattered by liquid droplets of the spray, this technique makes it possible to differentiate the liquid region from the vapor region. Captured images are processed and adjusted to eliminate undesired effects.

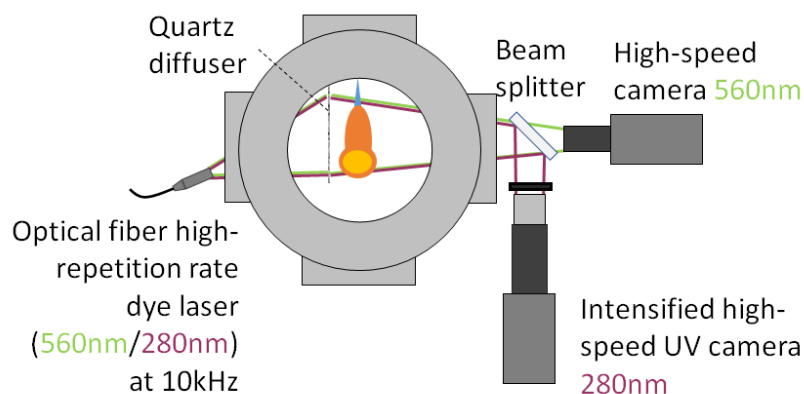


Figure 1. Schematic of the combustion vessel and optical equipment. [2]

Then, following Beer-Lambert's law, the optical thickness of the images can be calculated, which is used to calculate the projected fuel concentration later.

In order to check the number of injections necessary to obtain a representative ensemble average of the spray, several aspects were analyzed. First, once the time scale of the spray was adjusted and outliers eliminated, the standard deviation was analyzed. With this, it is verified how many injections are necessary to capture the fluctuations of the spray. Then, the confidence interval concerning the number of samples/injections used was studied. With these two analyses, a conclusion could be reached regarding the number of samples/injections required.

Once the projected average fuel concentration has been obtained, the inverse Abel transform is used. This transform links the radial concentration of a function with its line-of-sight function; it can be seen more clearly in Equation 1 and Figure 2.

$$f(r) = -\frac{1}{\pi} \int_r^{\infty} \frac{dF(y)}{dy} \frac{1}{\sqrt{y^2 - r^2}} dy \quad \text{Equation 1}$$

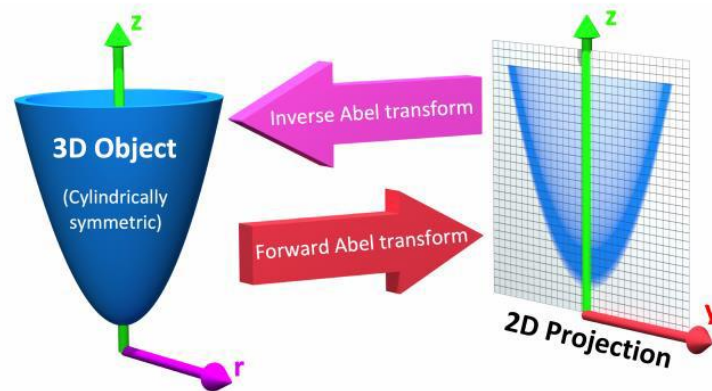


Figure 2. Schematic of the Abel transform. [3]

Before applying the transform to our data, its behavior was analyzed with several analytical equations, in addition to other experimental data provided by ECN. With what was learned from this previous analysis, the inverse Abel transform was applied to our data. And finally, the results are checked with the Rayleigh scattering planar concentration data provided by ECN.

4. Results

First, regarding the number of samples required, it was found that the standard deviation tended to stabilize around 30-40 samples. On the other hand, the confidence interval is reduced to 5-6% of the average value. Obviously, if more samples are added, the confidence interval will get smaller; however, the large costs involved in each additional sample means that this number should be kept as low as possible. Therefore, for this type of experiment, it was concluded that 30-40 were sufficient to capture the fluctuations of

the spray, while maintaining a sufficiently low confidence interval. In the illustration below it can be seen the confidence interval calculated for different numbers of samples.

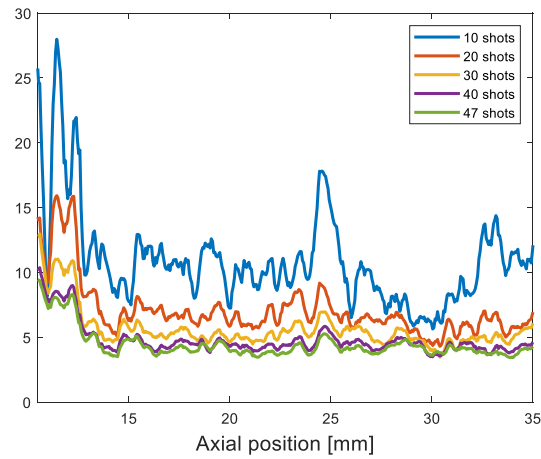


Figure 3 Confidence interval (%) of the optical thickness, at the centerline of the spray using different number of samples

The results of the inverse Abel transform to obtain the planar concentration can be seen in Figure 4. The first thing to note is that the calculated concentration is below the concentration measured by ECN, by around a factor of two. The hypothesis put forward by our group about the cause of this factor is the pressure dependence of naphthalene. This phenomenon will be investigated in the future work of the group, however, for this work, a correction factor of two is applied.

It is observed how the trend of the planar fuel concentration on the centerline of the spray matches with the Rayleigh scattering data. On the other hand, the concentration also matches for the axial plots. Although only four axial positions of the planar concentration have been represented in the figure, it was found that the rest of the positions also matched the data.

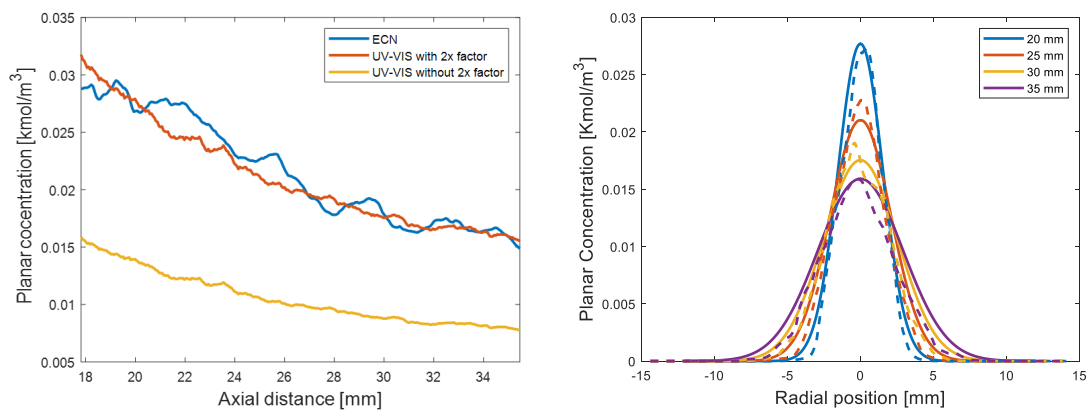


Figure 4. Validation of the transformed planar fuel concentration with respect to the ECN measurement at the center line of the spray (left) and at four axial positions (right).

5. Conclusions

First, it was found that the number of samples necessary to obtain an ensemble average that represents the fluctuations of the spray with a confidence interval of 5%, was 30-40 injections.

Second, while the pressure dependence of naphthalene remains to be checked, the transformed planar fuel concentration was found to match with the trend shown by the ECN data.

Finally, it was also verified that the uncertainty introduced by the inverse Abel transform is low when the resolution of the function is sufficient, tends to zero and has no sudden changes in it.

6. References

- [1] I. E. Agency, "CO2 emissions from fuel combustion," 2019.
- [2] C. Godbold, F. Poursadegh, O. Bibik, C. de la Camara Castillo and C. Genzale, "A multi-wavelength extinction imaging diagnostic for quantifying diesel spray mixing at engine-relevant conditions," ASME, 2020.
- [3] D. Hickstein, S. Gibson, R. Yurchak, D. Das and M. Ryazanov, "A direct comparison of high-speed methods for the numerical Abel transform," Review of Scientific Instruments 90, 2019

Table of contents

Chapter 1. Introduction	9
Chapter 2. Literature review	13
2.1 Measurement Techniques for Quantifying Air-Fuel Mixing in Diesel Sprays	13
2.1.1 Planar Measurements.....	13
2.1.2 Line-of-sight Measurements	17
2.1.3 Other limitations.....	20
2.2 Planar and three-dimensional reconstructions methods	21
2.2.1 Argonne methodology.....	21
2.2.2 Sandia interpolation method	22
2.2.3 Abel transform.....	23
Chapter 3. Experimental setup	27
3.1 Combustion vessel.....	28
3.2 Injector and fuel selection	29
3.3 Optical setup.....	30
3.4 Operating conditions	31
Chapter 4. Methodology	33
4.1 Ultraviolet-Visible Diffuse-Backlight Illumination (UV-Vis DBI) Imaging.....	33
4.2 Ensemble Averaging	37
4.2.1 Aligning the Time Records from Individual Injections.....	37
4.2.2 Elimination of Outliers	41
4.3 Inverse Abel transform	44
4.3.1 Testing synthetic data.....	44
4.3.2 Evaluation of Inverse Abel Transform on ECN Planar Spray Mixing Data	52
Chapter 5. Results	59
5.1 Determining a Statistically Relevant Ensemble Average.....	59
5.1.1 Standard deviation.....	60
5.1.2 Confidence interval	63
5.2 Inverse Abel transform applied to the UV-Vis DBI data	67

5.2.1 Correcting for spray pointing angle.....	67
5.2.2 Gaussian fit.....	69
5.2.3 Uncertainty analysis.....	76
Chapter 6. Conclusion.....	83
Chapter 7. References.....	85
APPENDIX I. Sustainable development goals.....	91

List of figures

<i>Figure 1. Schematic of the combustion vessel and optical equipment. [2]</i>	16
<i>Figure 2. Schematic of the Abel transform. [3]</i>	17
<i>Figure 3 Confidence interval (%) of the optical thickness, at the centerline of the spray using different number of samples</i>	18
<i>Figure 4. Validation of the transformed planar fuel concentration with respect to the ECN measurement at the center line of the spray (left) and at four axial positions (right).</i>	18
<i>Figure 5. Constant volume combustion vessel for Rayleigh scattering measurements. Source: Pickett et al. [6]</i>	15
<i>Figure 6. Rayleigh scattering image of a non-reacting spray from a constant volume vessel using a 532nm wavelength with a back-illuminated CCD camera. Source: Pickett et al. [6]</i>	16
<i>Figure 7. Optical setup for a Laser Extinction/Absorption technique using dual wavelengths. Source: Zhao and Ladommatos [21]</i>	19
<i>Figure 8. Raw images ratio for visible and ultraviolet, and equivalence ratio for liquid and vapor. Source: Suzuki et al. [10]</i>	20
<i>Figure 9. Abel transform. Source: Hickstein et al, 2019 [28]</i>	24
<i>Figure 10. Constant pressure continuous flow chamber. Source: Knox 2016 [33]</i>	29
<i>Figure 11. Optical setup. Source: C. Godbold et al. 2020 [32]</i>	31
<i>Figure 12. Beer-Lambert law illustration. Source Edinburgh Instruments [36]</i>	34
<i>Figure 13. Measured optical thickness of a vaporizing diesel jet back-illuminated by 280-nm diffuse illumination. Experimental conditions: 900K, 22.8 kg/m³, 1000 bar injection pressure, 3.5ms</i>	36
<i>Figure 14. Projected fuel vapor concentration example. [kmol/m²]. Experimental conditions: 900K, 22.8 kg/m³, 1000 bar injection pressure, 3.5ms</i>	37
<i>Figure 15. Comparison between two injections with different hydraulic delays, resulting in differences in start-of-injection timing. Time interval: 0.3ms</i>	38

<i>Figure 16. Selected region analyzed for determining the start-of-injection frame.</i>	<i>39</i>
<i>Figure 17. Comparison of the 150x11 pixels region for a frame without a spray (top) and a frame with a spray (bottom)</i>	<i>40</i>
<i>Figure 18. Identified start-of-injection frame for each measured injection.</i>	<i>41</i>
<i>Figure 19. Optical thickness comparison. Shot #13 is a standard value, while #40, #41, #42 and #91 are outliers.....</i>	<i>43</i>
<i>Figure 20. Inverse Abel transform test of a simple analytic function (Equation 11).....</i>	<i>45</i>
<i>Figure 21. Inverse Abel transform test of a simple analytical Equation 13.....</i>	<i>46</i>
<i>Figure 22. Inverse Abel transform for Equation 11 and Equation 13 with $a=1$.</i>	<i>47</i>
<i>Figure 23. Radial plot optical thickness at 15, 25 and 35mm from the nozzle. Experimental conditions: 900K, 22.8 kg/m³, 1000 bar injection pressure. 3.5ms</i>	<i>48</i>
<i>Figure 24. Inverse Abel transform for a Gaussian function.....</i>	<i>50</i>
<i>Figure 25. Inverse Abel transform error comparison for different resolutions. Gaussian function.....</i>	<i>51</i>
<i>Figure 26. Projected fuel concentration of Spray A based on the integration of existing planar Rayleigh scattering measurements. [kmol/m²] Experimental conditions: 900 K, 22,8 kg/m³, 1000 bar injection pressure.....</i>	<i>53</i>
<i>Figure 27. Measured planar fuel concentration(left) and Abel reconstruction of planar fuel concentration from line-of-sight integrated projected fuel concentration(right).[kmol/m³] Experimental conditions: 900 K, 22,8 kg/m³, 1000 bar injection pressure.</i>	<i>54</i>
<i>Figure 28. Comparison of measured planar fuel concentration and Abel reconstructed planar fuel concentration along the spray centerline of Spray A [kmol/m³] Experimental conditions: 900 K, 22,8 kg/m³, 1000 bar injection pressure.</i>	<i>55</i>
<i>Figure 29. Radial plot comparison between Abel reconstructed planar fuel concentration (solid line) and measured planar fuel concentration in Spray A (dashed line) at 20, 30, 40 and 50 mm from the nozzle. [kmol/m³]</i>	<i>56</i>

Figure 30. Standard deviation vs Number of shots used without the outliers. Two top plots are for the first set of 47 injections; two bottom plots are for the second set of 49 injections. Locations: centerline at 20 and 30 mm downstream of the injector nozzle. Time: 3.5ms.. 62

Figure 31. Lilliefors test for 40 raw images at 3.5ms. Yellow dots represent rejecting the null hypothesis. Blue dots represent not rejecting the null hypothesis. Edge of the spray is represented in red..... 64

Figure 32. Confidence interval (%), $t_{n-1; \alpha/2} \cdot s_x$, at the centerline, using different number of shots..... 66

Figure 33. Left image: radial position of the maximum value of measured optical thickness as a function of the axial position from the injector nozzle exit. Right image: pointing angle of the spray (red) vs horizontal line (black) for optical thickness at 3.5ms..... 68

Figure 34. Position of the maximum value for the rotated optical thickness..... 69

Figure 35. Gaussian fit optical thickness at 15, 25 and 35 mm from the nozzle. The solid line is the optical thickness, and the dashed line is the Gaussian fit..... 70

Figure 36. Inverse Abel transform of projected fuel concentration comparison between 400 and 1600 data points at 18 mm downstream. Planar fuel concentration [kmol/m³]..... 71

Figure 37. Planar fuel concentration obtained by the inverse Abel transform of the line-of-sight measurement of projected fuel concentration. [kmol/m³]..... 72

Figure 38. Validation of the predicted planar fuel concentration along the spray centerline using and inverse Abel transform against ECN Spray A planar Rayleigh scattering measurement..... 73

Figure 39. Planar fuel concentration at 20, 25, 30 and 35 mm from the nozzle. The solid line is the UV-VIS result, and the dashed line is the ECN data. 75

Figure 40. Radial plot of optical thickness plus estimate of the upper and lower bound in the mean optical thickness at 15 (left) and 30 mm (right) from the nozzle. The solid line is the measured optical thickness, and the dashed line is the gaussian fitted curve. Number of measurements used: 40..... 77

<i>Figure 41. Input and output of the inverse Abel transform for the UV-VIS DBI data and its boundaries at 15mm downstream of the injector nozzle.....</i>	<i>78</i>
<i>Figure 42. Input and output of the inverse Abel transform for the UV-Vis DBI data and its boundaries at 23.4 mm.....</i>	<i>79</i>
<i>Figure 43. Centerline planar fuel concentration comparison between ECN planar Rayleigh measurements and inverse Abel transform of UV-Vis DBI.....</i>	<i>80</i>
<i>Figure 44. Planar fuel concentration comparison for a radial plot at 20 mm from the nozzle</i>	<i>81</i>
<i>Figure 45. Planar fuel concentration comparison for a radial plot at 25 mm from the nozzle</i>	<i>82</i>

List of symbols and abbreviations

- C Calibration constant for optic setup
- DBI Diffuse Backlight Illumination
- Erf Gaussian error function
- $F(y)$ Projected density
- $f(r)$ Emission function
- I Received intensity
- I_0 Initial intensity
- I_l Incident laser intensity
- I_R Rayleigh scattering intensity
- n Number of samples
- N Number density of the gas
- r Radial distance
- s Standard deviation
- s_x Standard error
- t Transmissivity
- $t_{n-1; \alpha/2}$ T-distribution

UV Ultraviolet

Vis Visible

x_i Sample value

\bar{x} Mean

X_i Mole fraction

y Vertical distance

$1 - \alpha$ Level of probability

σ Variance

σ_i Scattering cross-section

τ Optical thickness

$\Pi_a(r)$ Rectangle function

μ Mean

Chapter 1. INTRODUCTION

Nowadays, emissions are an increasing concern for the world; in particular, carbon dioxide (CO₂) emissions is the topic of numerous investigations and articles. CO₂ is a significant greenhouse gas, which 24% of its global emission, is produced by the transport sector [1]. When similar diesel and gasoline engines are compared, diesel engines produce between 11 and 40% less CO₂ emissions [2]. For this reason, and others such as higher fuel economy, lower maintenance and more produced torque, diesel engines are continued to be researched and developed. Nevertheless, there are other gases that even though there are emitted in fewer quantities than CO₂, they have a more significant impact on the environment. For instance, methane has a Global Warming Potential of 28, which means that one ton of methane has the effect of emitting 28 tons of CO₂; furthermore, NO₂ has a GWP of 265 [3]. As a result, regulations in the sector are getting tighter and more challenging to accomplish each time.

It is crucial to keep reducing emissions of internal combustion engines; the two main groups of emissions control techniques are aftertreatment and in-cylinder. Aftertreatment techniques attempt to reduce emissions once the exhaust gases have left the combustion system, while in-cylinder techniques aim to produce fewer pollutants by optimizing combustion. While aftertreatment systems can be complex and expensive, in-cylinder techniques require a fundamental understanding of the in-cylinder mixing and combustion processes. As a result, many research efforts have focused on developing quantitative measurements of in-cylinder mixing and combustion. For example, Sandia National Laboratories approached a reduction on NO_x and particulate emissions by the use of

advanced compression ignition engines [4], which required a detailed understanding of the fuel distribution, thermal stratification, fuel effects and low-temperature combustion understanding. Another relevant paper [5], studied the performance and emission characteristics of Homogeneous Charge Compression Ignition (HCCI) engines using a CFD analysis to quantify mixture homogeneity and spatial distribution of fuel.

Many experiments and investigations have shown how closely coupled emissions are to air-fuel mixing. Flame temperature, pollutant formation, unburned fuel emissions and combustion efficiency can be affected by the mixture distribution [6]. There are two primary pollutants in diesel engines: nitrogen oxides (NO_x) and soot. Soot can be reduced with the use of biodiesel; however, it is usually linked to an increase in NO_x . Many theories have emerged trying to identify the increase of NO_x emissions with biodiesel fuels, as many factors have been shown to affect the production of NO_x emissions by biodiesel fuels. [7] Mueller et al. showed [8] that a highly plausible reason for the increased NO_x in biodiesel fuels was charge-gas mixtures that are closer to stoichiometric during ignition. Other investigations with diesel have indicated that soot is highly linked to the temperature of combustion and fuel mixing. Pickett et al. [9] concluded that by increasing the injection pressure, the soot in a fuel jet could be decreased, however, if the ambient gas density increases, a non-linear increase takes place in the soot levels of a fuel jet. The overall trends showed a correlation with the cross-sectional average equivalence ratio at the lift-off length. These are just two of the multiple examples that show how air-fuel mixing problems are linked to emissions.

To improve fundamental understanding of the coupling between emissions and mixing in diesel sprays, a new optical technique for the measurement of air-fuel mixing in diesel sprays, Ultraviolet-Visible Diffuse Back-Illumination (UV-Vis DBI), is currently under development in our lab. The main benefit of UV-Vis DBI is the possibility to measure fuel vapor concentration and liquid droplets simultaneously. Furthermore, UV-Vis DBI can be used in near-spray measurements as it does not have the interferences from the liquid that other common techniques have. The principle on which this technique is based is the absorption of UV light by fuel vapor and scattering of visible light by fuel droplets [10].

This work addresses three fundamental goals related to the UV-Vis DBI technique. First, the experiment set in our lab deals with a highly turbulent flow field, a diesel spray. Thus, it is crucial to determine an accurate ensemble average flow that represents the behavior of the spray. To do so, a statistical analysis will be conducted for the data gathered. Second, enable validation for the measurements of this new UV-Vis DBI technique with planar measurements. This new technique that is being developed in our lab is a line-of-sight diagnostic. Therefore, our results must be transformed into a planar fuel concentration field. For this purpose, the inverse Abel transform will be used and analyzed. Additionally, the propagation of an error in the average measurement through the inverse Abel transform will be evaluated.

Chapter 2. LITERATURE REVIEW

For a better understanding of how to reduce emissions with in-cylinder techniques, numerous diagnosis and measurements procedures have been developed. Some of the most used techniques are Laser Rayleigh scattering (LRS) [6], Spontaneous Raman Scattering (SRS) [11] and Laser-Induced Fluorescence (LIF). [12] These three techniques are used mainly to measure the vapor concentration of the spray. Other techniques such as the Ultraviolet-Visible Diffuse Backlight Illumination, which will be the one used in this work, are capable of measuring the liquid and vapor region of the spray simultaneously. Measurement techniques can be classified into two main groups: planar measurements and line-of-sight measurements.

2.1 MEASUREMENT TECHNIQUES FOR QUANTIFYING AIR-FUEL MIXING IN DIESEL SPRAYS

2.1.1 PLANAR MEASUREMENTS

One of the planar imaging techniques that has achieved quantitative mixing measurements is Rayleigh Scattering. This technique is based on the elastic scattering of the incident light caused by the interaction with gas particles; thus, scattered and incident light have the same wavelength. There are two main advantages of using this technique. First, a tracer is not

required because the elastic scattering occurs directly from the fuel molecule. Second, the signal intensity is directly proportional to the molecular number density.

The measuring principle of Rayleigh scattering has been widely described in some publications such as references [13] and [14]. The main equation that describes the Rayleigh scattering intensity, I_R was described as shown below by F. Robben. [15]

$$I_R = CI_l N \sum_i X_i \sigma_i \quad \text{Equation 2}$$

Here, C is the calibration constant for the optics, I_l the incident laser intensity, N the number density of the gas, X_i the mole fraction and σ_i the scattering cross-section.

Following this principle, Espey et al. [16] achieved quantitative fuel vapor concentration in an optically accessible diesel engine. Then following the same methodology, Picket et al. [6] obtained quantitative mixing measurements in a vaporizing diesel spray at a constant volume vessel. Their validation was based on the relationship between soot formation in diesel jets and the equivalence ratio. Furthermore, at reference [17] they used quantitative Rayleigh measurements to identify mixture fraction and to evaluate the accuracy of a mixing prediction model.

The experimental setup used in these two projects, which also is a common arrangement, was an optically accessible constant volume vessel simulating diesel engine conditions. A schematic of the arrangement can be seen in Figure 1.

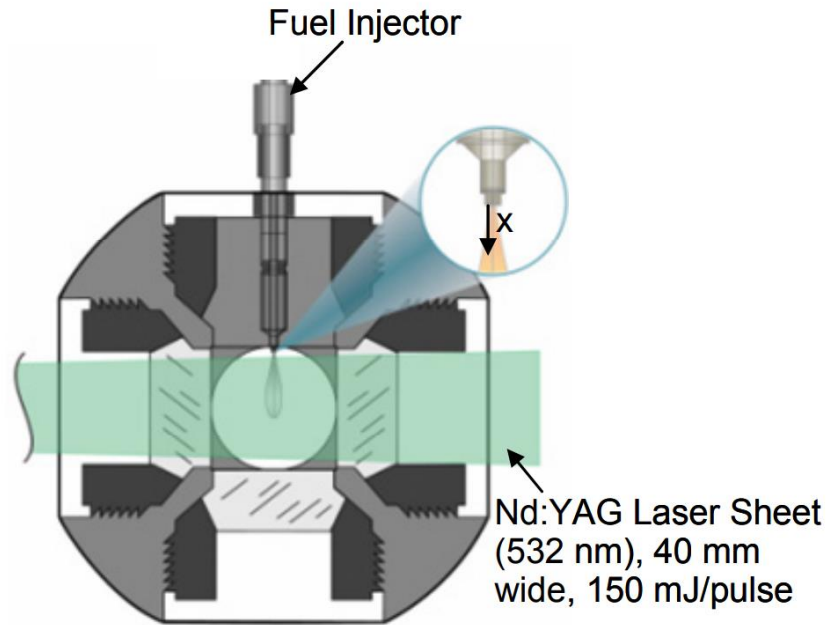


Figure 5. Constant volume combustion vessel for Rayleigh scattering measurements. Source: Pickett et al.

[6]

An ND-YAG laser with a 532nm wavelength is commonly used. The laser beam is passed through different optics equipment to obtain a collimated planar sheet. This sheet is typically 40 mm wide and 300 μm thick. The planar sheet is passed through the center of the spray, and the high-speed cameras are placed perpendicularly to it. Back-illuminated CCD cameras are preferred rather than intensified CCD cameras, due to their higher resolution, better dynamic range, quantum efficiency and linearity. However, intensified CCD cameras are required for reacting sprays. An example of the images obtained by the described setup using a back-illuminating CCD can be observed in Figure 2.

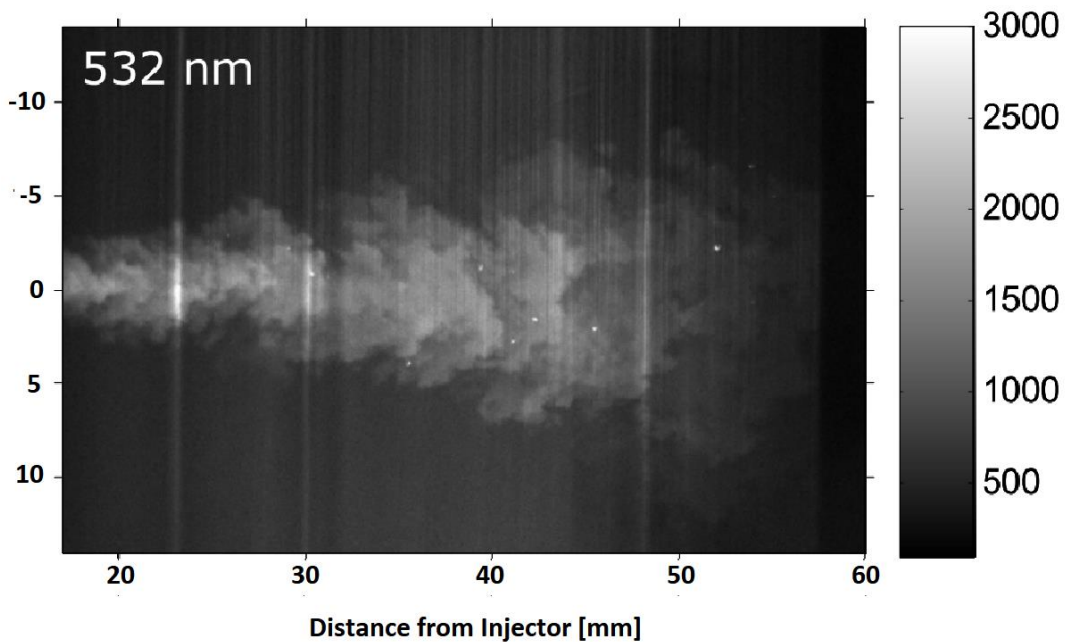


Figure 6. Rayleigh scattering image of a non-reacting spray from a constant volume vessel using a 532nm wavelength with a back-illuminated CCD camera. Source: Pickett et al. [6]

This figure is the raw intensity map obtained from the cameras. In it, there are some interferences such as particles, beam steering and background noise that must be addressed.

Rayleigh scattering can be affected by particles and Mie scattering, causing severe interferences. Therefore, filters and special low-particles fuel must be used to reduce this effect. Furthermore, even with all these precautions, particles can appear in the collected data. Then, the data requires some post-processing, such as median filtering, to remove undesired particles; Pickett et al. [6] used a 13x13 median filter for their data, which introduced less than 1% of bias error.

Another common issue for Rayleigh scattering is beam steering, which needs to be corrected by filtering or interpolations methods. Other factors that must be considered for Rayleigh measurements are the placement of the laser sheet, accurate measurement, and correction of the background.

After post-processing and filtering the images, the equivalence ratio can be obtained using the ambient-to-fuel number density. The main restriction of the resulting air-fuel ratio is the unavailability to obtain either qualitative or quantitative data near the nozzle. The closest to the nozzle these techniques can measure is limited to the region where only vapor phase exists, for Espey et al. [16] Rayleigh Imaging, the data shown is beyond 27 mm downstream; for the ECN Rayleigh data, it is beyond 17.8 mm. [17]

2.1.2 LINE-OF-SIGHT MEASUREMENTS

On the other hand, on line-of-sight measurements, a source produces a laser beam that goes through the spray and its received by a high-speed camera. One of the most relevant line-of-sight techniques is the Laser Extinction Absorption technique. In 1981, Charpyvy [18] proposed to use two simultaneous wavelengths in a laser extinction experiment to measure liquid and vapor concentration. This technique was then probed by Suzuki et al. [10] in 1993.

It is based on the different absorption/scattering properties of the liquid and vapor; visible light is only attenuated by the scattering of liquid droplets, while ultraviolet light is attenuated by the scattering and absorption of liquid droplets, and by the absorption of vapor

fuel. Thus, the transmissivity, t , of each wavelength can be represented by the following equations.

$$t_{visible} = t_{Liquid,scattering} \quad \text{Equation 3}$$

$$t_{UV} = t_{Liquid,scattering} + t_{Liquid,absorption} + t_{Vapor,absorption} \quad \text{Equation 4}$$

However, the attenuation of ultraviolet light by liquid absorption was shown to have a low contribution to the total transmissivity [19] [20], then Suzuki [10] probed it to be neglectable. As a result, the transmissivity of the vapor region can be expressed by the difference between the transmissivity of the UV and the transmissivity of the liquid scattering. Then Equation 4 can be expressed as shown below.

$$t_{Vapor,absorption} = t_{UV} - t_{vis} \quad \text{Equation 5}$$

Therefore, if the information for both visible and ultraviolet light is captured, then the liquid scattering and vapor absorption can be obtained in Equation 3 and Equation 5.

Then each wavelength is captured by a high-speed camera. Therefore, it can be differentiated which region corresponds to liquid or vapor. This enables much near nozzle measurements, which is a common limitation of other techniques.

A typical optical setup used for a dual-wavelength measurement is shown below.

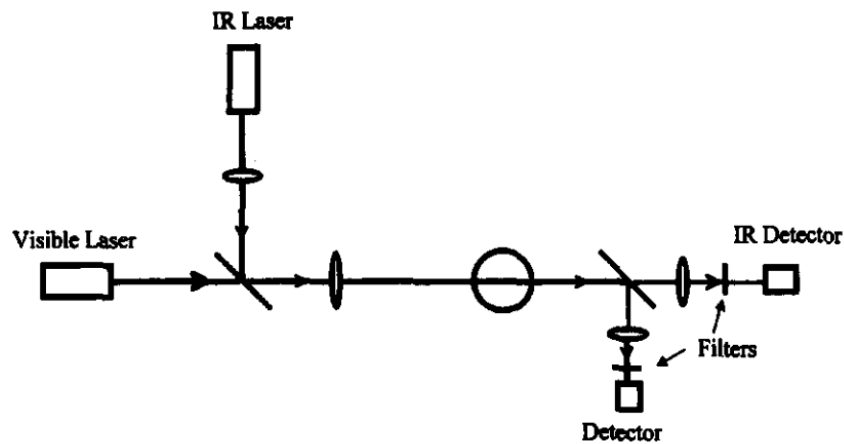


Figure 7. Optical setup for a Laser Extinction/Absorption technique using dual wavelengths. Source: Zhao and Ladommatos [21]

As it can be seen in Figure 7, both wavelengths passed through the vessel (represented at the middle by a circle) and then each wavelength is separated and captured by different cameras. In Figure 7, the combination selected is a visible-infrared setup; however, the most common setup is the visible-ultraviolet. The typical wavelengths used are 560 nm for the visible and 280 nm for the ultraviolet, induced by an ND-YAG laser.

Then, the mass concentration and equivalence ratio can be calculated by processing the data captured. One example of the first images captured by this technique was printed in SAE paper 930863 [10], Figure 8. However, the results obtained with this technique are line-of-sight measurements; thus, to compare and validate them with other planar measurements, a transformation must be performed.

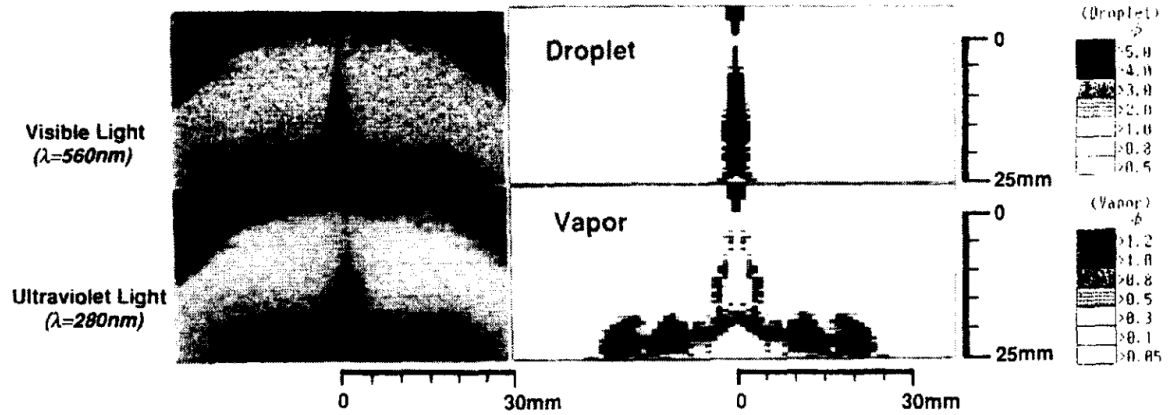


Figure 8. Raw images ratio for visible and ultraviolet, and equivalence ratio for liquid and vapor. Source:

Suzuki et al. [10]

2.1.3 OTHER LIMITATIONS

One key limitation in mixing measurements is that the number of shots available is often limited to 20-30 images. Facilities are often limited to a low repetition rate; in addition, many of the images taken cannot be used due to interferences and contamination. When results are presented, all the images are ensemble-averaged to obtain a representative picture of the spray. However, if the number of images is low, the uncertainty increases. This limitation is addressed in this work thanks to the high repetition rate and availability of our setup.

2.2 PLANAR AND THREE-DIMENSIONAL RECONSTRUCTIONS

METHODS

With line-of-sight techniques, the data obtained is an intensity image proportional to the absorption of light by the fuel spray. Then an optical thickness image can be obtained, furthermore, with some additional calculations, the projected concentration can be calculated. However, the majority of data of other mixing experiments are planar measurements. Therefore, to compare the results of line-of-sight measurements with planar measurements, a reconstruction/transformation method must be applied. Several tomography methods can be applied to reconstruct a planar or three-dimensional image. For reconstructing the spray concentration, multiple viewing angles are needed; however, other techniques such as the inverse Abel transform are able to reconstruct the spray when the data is limited to only one viewing angle.

2.2.1 ARGONNE METHODOLOGY

Argonne described and tried a tomography method that is explained by Kastengren et Al. [22] They used X-ray measurements at several viewing angles to reconstruct the density distribution of the spray. X-ray measurements provide information about the projected fuel distribution just as the UV-VIS does. Argonne used the ensemble average of 32 injections for four different angles. This is a very limited number of viewing angles for reconstruction, with the filtered back-projection method 50-80 viewing angles will be needed. [22] [23]

Argonne reconstruction algorithm is based on fitting the projected data into gaussian and constant density models, then some parameters such as width and displacement of the model peak value, finally, after another curving fitting with these parameters, the density distribution is calculated. They conclude that this method can be useful to observe the mean behavior of the spray; the uncertainty was estimated to be 30%, but more viewing angles are required to determine the density distribution accurately. This method was later used by Kastengren et Al. 2014 [24] for studying the asymmetry of the spray.

2.2.2 SANDIA INTERPOLATION METHOD

Recently, another tomography method was described for a Spray G plume by Weiss et al. [25]. This method used three different views from an extinction imaging technique. The objective was to reconstruct a 3D model of the plume, using the data from the projected liquid volume.

The setup used at Sandia National Laboratories was similar to the one by our group at the Spray Physics and Combustion Engine Research Lab, a Diffuse Backlight Illumination Extinction Imaging (DBEI) technique with a 519 nm pulsed LED. From the data they acquired, a liquid volume fraction was extracted using the one-dimensional control-volume jet model by Musculus and Kattke, 2009. [26] To test the reconstruction method before the experimental extinction data was used, synthetic data was created. The procedure consisted of creating a 180° degree sinogram for each axial position by the use of only three different viewing angles. The points between the three viewing angles were interpolated to obtain the

full 180° plot. Then, the sinograms were inputted to the inverse Radon function to reconstruct the 3D model. This experiment concluded that the procedure could determine the general plume directions in the three dimensions. However, this technique cannot be used to reconstruct an asymmetric spray due to the interpolation made, the limited angles and additional uncertainties.

2.2.3 ABEL TRANSFORM

The Abel transform is an integral transform proposed by Niels Henrik Abel in 1826 in "Journal für die reine und angewandte Mathematik" [27]. A projected density function can be transformed from an emission function. The Abel forward transform is defined by

$$F(y) = 2 \int_y^{\infty} \frac{f(r)r}{\sqrt{r^2 - y^2}} dr \quad \text{Equation 6}$$

Where $F(y)$ is the projected intensity, $f(r)$ the emission function, r the radial distance, and y the vertical coordinate. The figure (Figure 9) created by Hickstein et al. [28] illustrates this transform

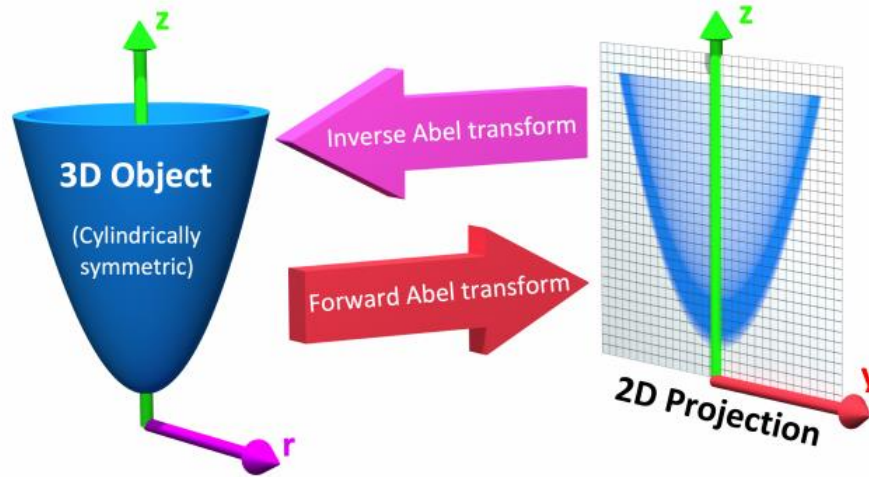


Figure 9. Abel transform. Source: Hickstein et al, 2019 [28]

Also, the emission function can be reconstructed using the projected density through the inverse Abel transform, defined by

$$f(r) = -\frac{1}{\pi} \int_r^{\infty} \frac{dF(y)}{dy} \frac{1}{\sqrt{y^2 - r^2}} dy \quad \text{Equation 7}$$

However, these analytical equations cannot be applied directly to experimental data due to some limitations. First, the data acquired in experiments is discrete, while Equation 6 and Equation 7 require continuous data. Second, both equations present a singularity when $y=r$, as the denominator goes to zero.

2.2.3.1 Numerical methods for Abel transform

Therefore, to evaluate the Abel transform for experimental data, numerical methods are required. There are several deconvolution methods to perform the inverse Abel transform, the most common ones, described by Dasch in 1992 [29], are:

- **Three-Point Abel Deconvolution.** This method uses matrix-algebra operations, dividing the integral into segments around each point, using only the projections adjacent to it.
- **Two-Point Abel Deconvolution.** This method is a simplification of the Three-Point Abel Deconvolution. It also breaks the integral into segments around each point, but only uses two projections.
- **Onion Peeling Deconvolution.** It is the simplest method, similar to the Two-Point Abel Deconvolution but uses rings of constant property between each point to calculate the integral.

Between these three methods, the Onion Peeling Deconvolution and the Two-Point Abel Deconvolution can be inaccurate when dealing with sharp edges, especially the Onion Peeling method that can be twice as noisy as the Three-Point method. Also, Hickstein et al. [28] included these three methods in a numerical Abel transform comparison paper. Their results showed that the three-point method provides the lowest error, lowest noise, and also one of the fastest computational transformation time.

Chapter 3. EXPERIMENTAL SETUP

There are hundreds of mixing measurements experiments, and each of them makes essential progress for the knowledge and improvement of engines. However, development is much more powerful if it is done as a group or community. This is not always simple to do; therefore, it is crucial to rely on organizations and working groups. The reference association for international collaboration in combustion engines is ECN (Engine Combustion Network). It includes members such as Sandia National Laboratories, Bosch, Universidad Politecnica de Valencia, Caterpillar. Their objectives are:

- Provide data sets for model validation and advancement understanding [30]
- Create a collaborative place to compare and share results [30]
- Provide future research priorities. [30]

For diesel engines, ECN provides some experimental reference conditions labelled as Spray A, B, C and D. Each of them with different injector configuration and boundary conditions. In this work, we will target Spray A and will try to reproduce all the conditions as close as possible. This spray configuration has been researched by many institutes such as Sandia, IFPEN, Universitat Politecnica de Valencia (CMT-Motores Termicos), Caterpillar, and Eindhoven University of Technology. [31]

For these reasons, the group chose to replicate Spray A in order to compare and validate data against the one posted by the ECN. In addition, the findings of our group can contribute to the network.

The experimental setup used by our group consisted of a test chamber, a laser, two high-speed cameras and additional optical equipment. The experimental facility was provided by the Spray Physics and Engine Research lab at Georgia Institute of Technology. The experimental setup and operating conditions were the same as the extinction imaging experiment described by C. Godbold et al. [32].

3.1 COMBUSTION VESSEL

The test chamber is a constant pressure continuous flow vessel. The reason for using this chamber is to simulate combustion conditions but without the complications of a real cylinder or a whole engine. The vessel can reach up to 100 bar pressure and 950K temperature. High-pressure gas is introduced through the bottom, where two heaters raise its temperature. Then the high-pressure high-temperature gas enters the main chamber where the injector is mounted. The main chamber is accessible through four removable windows, two of them equipped with quartz glass to allow light to go through it.

The gas used was 100% nitrogen in order to avoid combustion; the conditions we targeted was a non-reacting spray. This allowed us to examine the behavior and trend of the spray with no interference of the combustion.

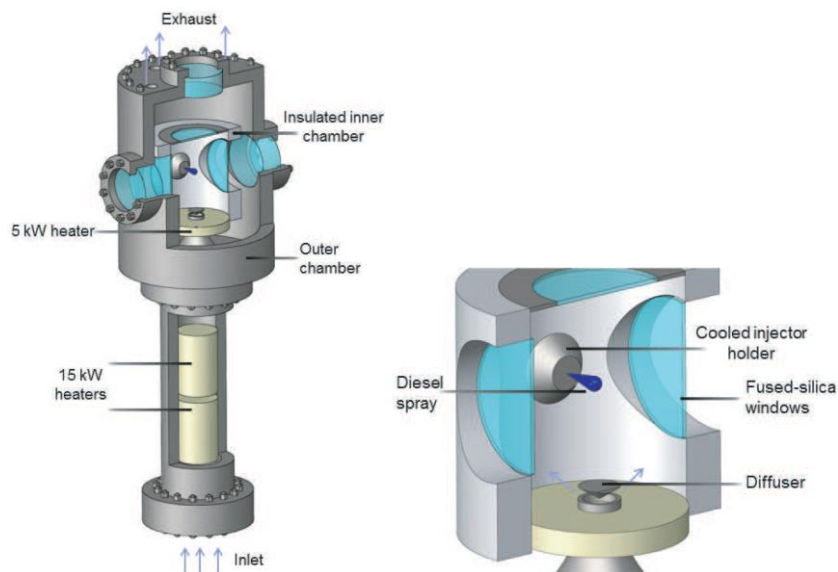


Figure 10. Constant pressure continuous flow chamber. Source: Knox 2016 [33]

3.2 INJECTOR AND FUEL SELECTION

The injector attached to the vessel in this project was a Bosch CRI3-20 ks1.5 single orifice injector with a 90 μm diameter.

The fuel used was a mixture composed of 99.25% mole dodecane and 0.75% mole naphthalene. The use of dodecane is common in research especially when Spray A condition is targeted. On the other hand, naphthalene was used as the aromatic tracer due to its suitable characteristics. The naphthalene absorption coefficient was widely described by Grosch et al. [34]; it does not have a large temperature or pressure dependence for a 280 nm at 800K as described by Orain et al. [35]. Also, naphthalene has a very similar boiling point to dodecane.

3.3 OPTICAL SETUP

This work employed a new line-of-sight air-fuel mixing diagnostic, currently under development in our lab, referred to as Ultra-Violet-Visible Diffuse Back-Illumination (UV-Vis DBI). Two illumination wavelengths were used, a 280 nm and a 560 nm, for them a frequency-double ND-YAG laser was used as the pump laser for a rhodamine 466 dye-cell, the output power and frequency were 2W and 10kHz respectively. Both wavelengths were carried through an optical fiber to the window and then allowed to expand onto a quartz diffuser. As a result, the scattered incident light created a diffused backlight area of illumination. At the exit of the vessel, the two wavelengths were separated by a 3" Diameter x 0.375" thickness dichroic mirror placed at 45°, which transmitted wavelengths above 532nm and reflected wavelengths below 300nm. Next, each wavelength passed through a filter; a 580nm band-pass Thorlabs UV filter and a Hicatt intensifier with a 600V gain for the 280 nm; and a neutral density filter with a 0.5 OD for the 560 nm wavelength. Finally, each wavelength was captured by a high-speed camera, the Photron SA-X2, using a 100mm focal length lens with an f/2.8 for the UV and a 70-250mm focal length with an f5.6 for the visible light. The sampling frequency of the cameras was 9.9 kHz at a resolution of 1024x1024 pixels, resulting in an image resolution of 0.06 mm/pixel.

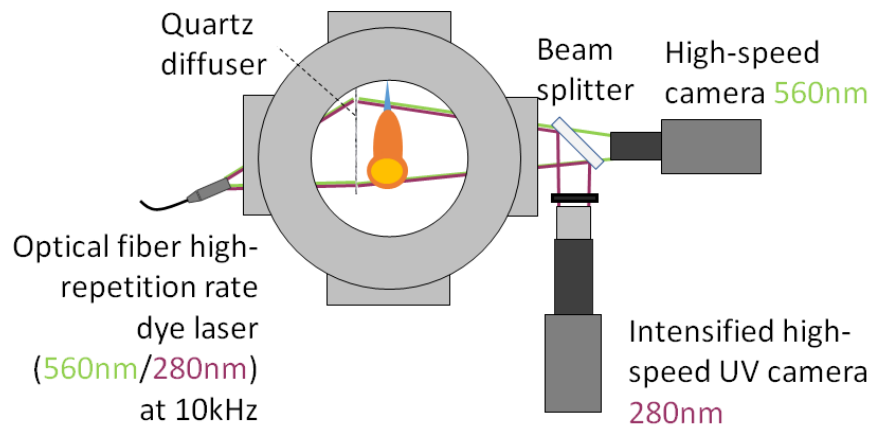


Figure 11. Optical setup. Source: C. Godbold et al. 2020 [32]

3.4 OPERATING CONDITIONS

The operating conditions were selected based on the conditions of Spray A described by ECN (Engine Combustion Network), to compare the results with the available data. The operating conditions are shown below.

- Chamber Temperature: 900K
- Chamber Pressure: 60 bar
- Laser Wavelengths: 280 nm and 560 nm
- Ambient gas: N₂
- Fuel Pressure: 1000 bar
- Fuel: 99.25% mole dodecane, 0.75% mole naphthalene
- Injector Tip Temperature: 373 K

- Commanded Injection duration 3 ms
- Imaging resolution 1024x1024 pixels
- Imaging frequency 9.9 KHz
- Recording duration: 5.7ms

Chapter 4. METHODOLOGY

The method used in this project had three major steps. First, the UV-Vis DBI imaging is explained; this technique is based on the Beer-Lambert law. Thanks to this law, the optical thickness and later, the projected concentration of the images can be calculated. Second, the data is prepared for the ensemble average, which requires aligning the time records of each shot, as well as removing possible outliers. Finally, the inverse Abel transform is discussed, using both synthetic data and ECN data from other experiments.

4.1 ULTRAVIOLET-VISIBLE DIFFUSE-BACKLIGHT ILLUMINATION (UV-VIS DBI) IMAGING

The images obtained through this UV-Vis DBI technique are line-of-sight measurements. It is measured how much light is obtained after passing through the diesel spray. The intensity received at the camera depends on original intensity produced and the amount of "interferences" light encounters through its path. In other words, the incident light is attenuated through the spray by the effect of absorption and scattering of the spray. If the scattering effect is known to be zero, then the extinction measurements are only dependent on absorption. Here is where the main advantage of the UV-Vis DBI takes place. With the visible light, the information about the liquid region of the spray is known. Then, with the ultraviolet light, the vapor plus liquid region is specified. After, the liquid region of the spray

is subtracted from the ultraviolet images. As a result, the region only containing vaporized fuel-ambient mixtures can be calculated. In this region, we can assure there is no Mie-scattering effect, so all the light is only affected by absorption; the following Beer-Lambert law can be applied.

$$\frac{I}{I_0} = e^{-\tau} \quad \text{Equation 8}$$

Where I is the received intensity, I_0 the initial intensity and τ the optical thickness. A general illustration of Beer-Lambert law can be seen in Figure 12.

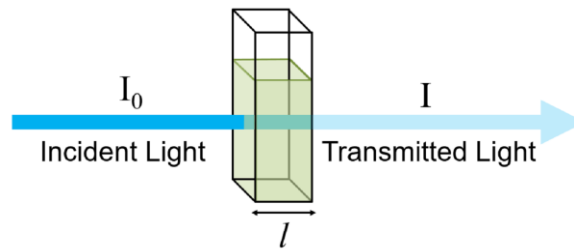


Figure 12. Beer-Lambert law illustration. Source Edinburgh Instruments [36]

By taking logarithms, the optical thickness can be derived.

$$\tau = -\log \left(\frac{I}{I_0} \right) \quad \text{Equation 9}$$

Equation 9 was the one used to calculate the optical thickness in this project. However, to address background and illumination intensity fluctuations, additional adjustments and

filtering were applied. These correction factors are described in further detail by Godbold et al. in [32].

For this project, 100 shots were captured in two sets of 50 shots. Each shot consisted of 56 frames corresponding to 5.6ms, 42 of them corresponding to the hydraulic injection. The additional frames captured the background prior to the injection, which was useful for the image processing; and the end of the injection when the injector was no longer infusing fuel, to ensure the whole injection was captured. The images were saved in a ".tif" format. The software selected to view and process the data was Matlab.

For each injection, one initial background frame without spray was captured; this was used to quantify the reference intensity, I_o , at each pixel in the frame. Then, for each frame in the injection time record, Equation 9 is applied to calculate the local optical thickness at each pixel. An example result is shown in Figure 13.

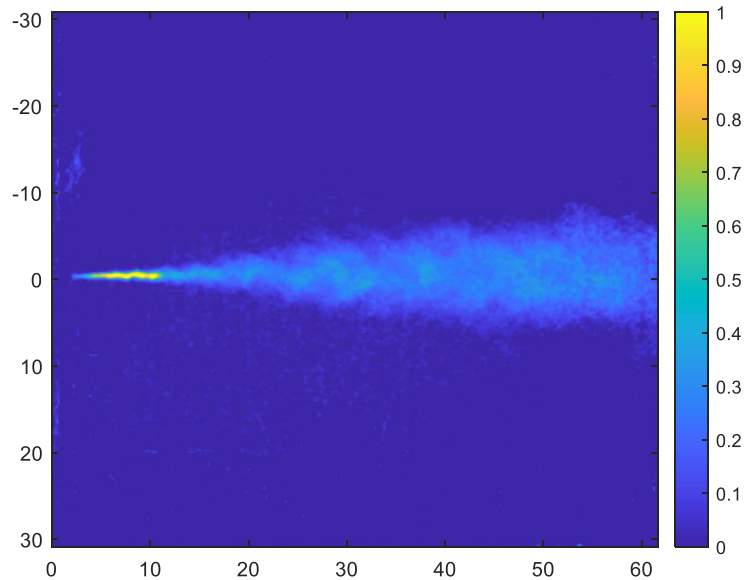


Figure 13. Measured optical thickness of a vaporizing diesel jet back-illuminated by 280-nm diffuse illumination. Experimental conditions: 900K, 22.8 kg/m³, 1000 bar injection pressure, 3.5ms

Once the instantaneous optical thickness is determined, the projected fuel concentration can be calculated. There are two additional parameters needed: the absorption coefficient and the naphthalene fraction. The naphthalene absorption coefficient is well characterized as it has been measured by both Grosch et al. [34] and Orain et al. [35]; at this project, for the 280 nm wavelength, we used a 1.255×10^{-17} cm²/molecule absorption coefficient based on reference [34]. Then, the projected concentration can be calculated as shown below.

$$\frac{\tau}{\text{absorption coefficient} \cdot \text{naphthalene fraction}}$$

Equation

10

The projected concentration shown in Equation 10 was calculated for every optical thickness image individually. An example is shown in the figure below.

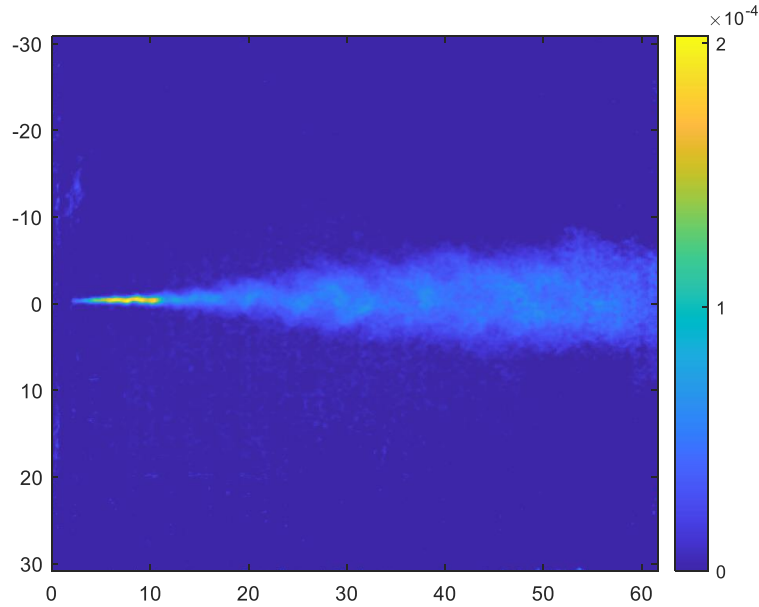


Figure 14. Projected fuel vapor concentration example. [kmol/m^2]. Experimental conditions: 900K, 22.8 kg/m^3 , 1000 bar injection pressure, 3.5ms

4.2 ENSEMBLE AVERAGING

4.2.1 ALIGNING THE TIME RECORDS FROM INDIVIDUAL INJECTIONS

Due to variation in the hydraulic delay time between the electronically commanded start-of-injection and the first moment of liquid injection from the nozzle, the imaging frame at which the injection started was not the same for all the injections; it varied between frame 2 and 3, producing a variation in the start-of-injection time by approximately $70 \mu\text{s}$. In Figure 15, we

can observe an example of an injection (shot 1) which injection starts at frame 2, and another one (shot 2) that starts at frame 3.

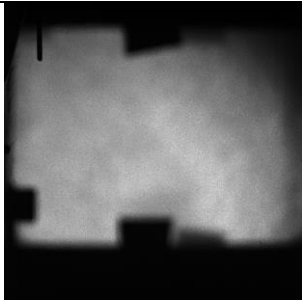
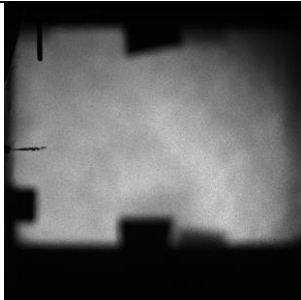
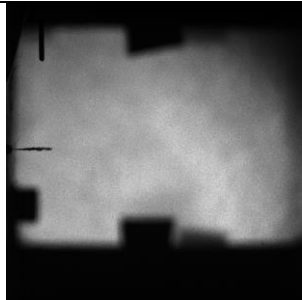
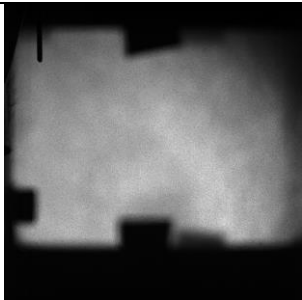
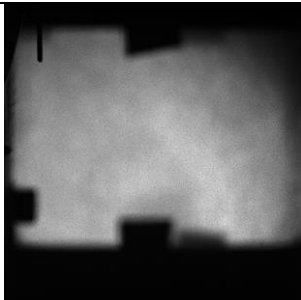
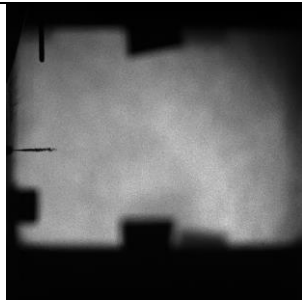
	Frame 1	Frame 2	Frame 3
Shot 1			
Shot 2			

Figure 15. Comparison between two injections with different hydraulic delays, resulting in differences in start-of-injection timing. Time interval: 0.3ms

In order to accurately ensemble average data from multiple injection realizations, it is essential to align the relative timing of each data set with respect to the start of injection. This was done by developing an automated processing routine to identify at which shots the injection started at frame 2 and which at frame 3. This check was done using the 560-nm

back-illumination images because they were brighter and higher contrast than the 280-nm images.

To identify the start-of-injection time for each injection, a processing routine was developed to monitor the injector nozzle region for a change in intensity signal. For each injection, the intensity of all the 56 frames was analyzed to make sure we identify the start of the injection even if it occurred at a frame different from the second and third frame we initially observed. For each frame, a region of 150x11pixels (9x0.66mm) near the injector tip was analyzed, this region is shown in Figure 16.

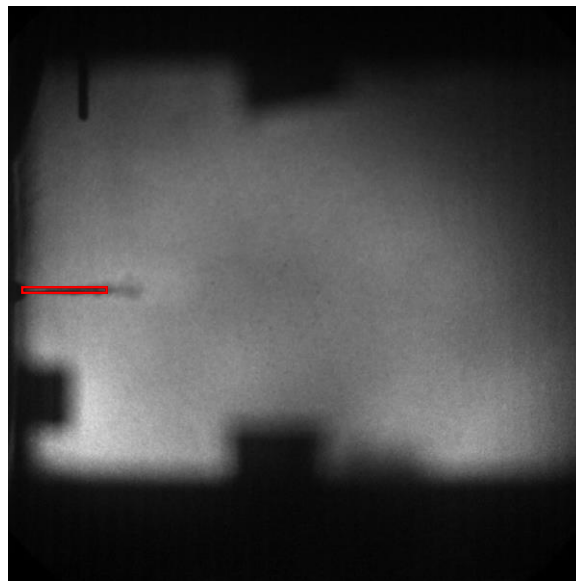


Figure 16. Selected region analyzed for determining the start-of-injection frame.

Then the intensity of this region was averaged; images with no spray were brighter, so its average was higher than the average of images with a spray.



Figure 17. Comparison of the 150x11 pixels region for a frame without a spray (top) and a frame with a spray (bottom)

The average intensity of each frame was compared with the previous frame and a threshold set at 1400 in the intensity scale; as a reference, a background image had an average of 2000 and the images with an initial spray 1200. The initial injection frame was determined when the average intensity of the frame was lower than the previous frame and lower than the threshold. The threshold was set by empirically testing several values and verifying the accuracy of the detected start of injection with visible inspection of the images.

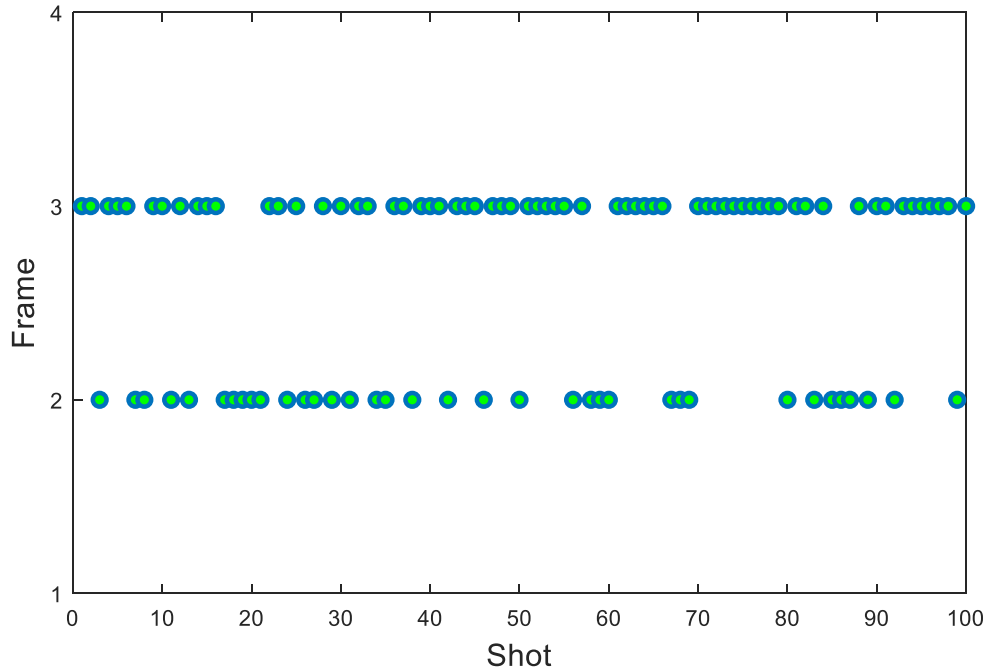


Figure 18. Identified start-of-injection frame for each measured injection.

The final classification can be observed in Figure 18. Thirty-six shots started on frame 2, and 64 started on frame 3. This graph set the time zero for each injection so that all shots can be accurately ensemble averaged at a given time.

4.2.2 ELIMINATION OF OUTLIERS

After the optical thickness was calculated, an additional issue was identified, outliers. The optical thickness was revised, and four shots had significantly higher values for the whole

spray injection duration. This difference in values was distinguishable even by visual comparison of the optical thickness images.

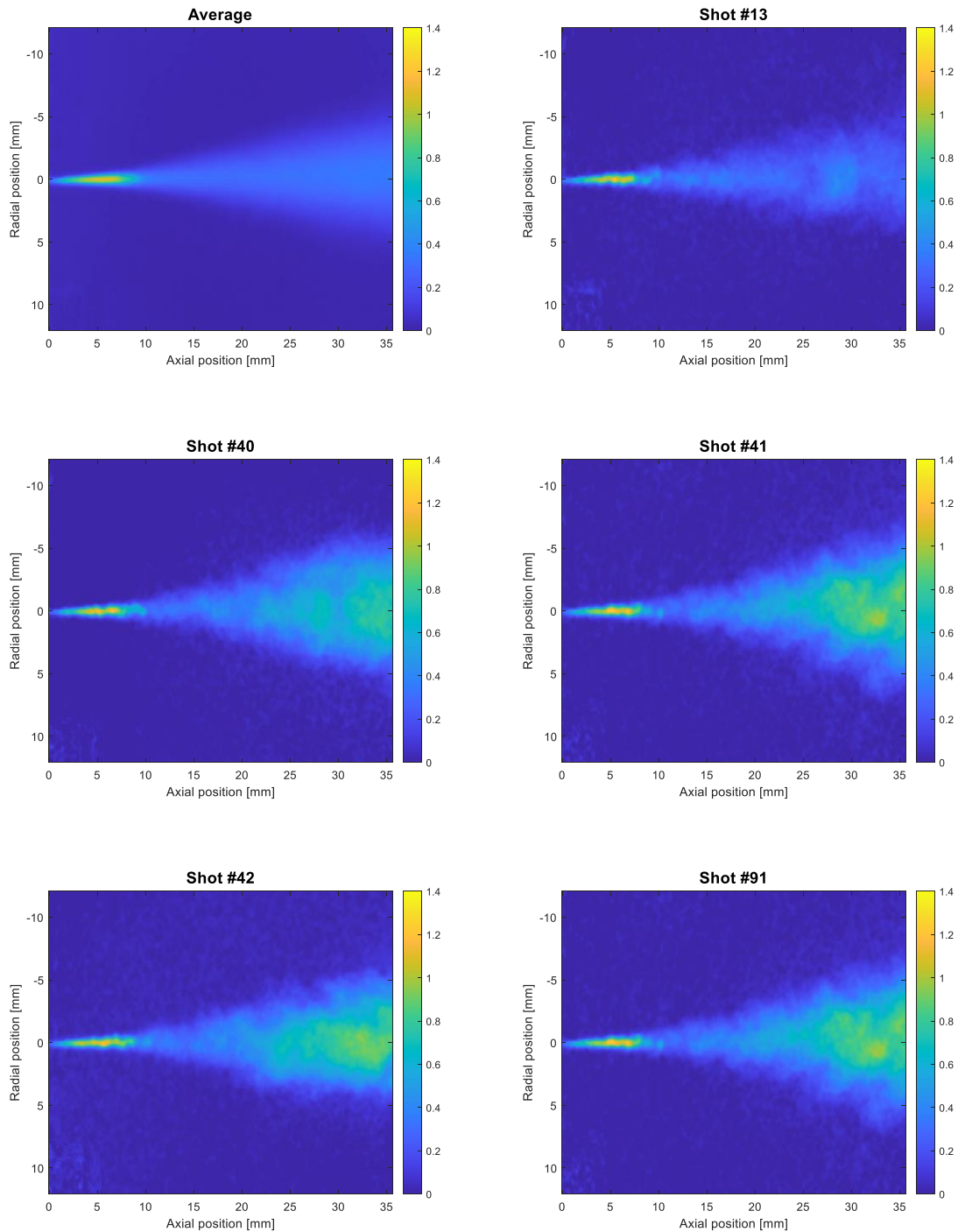


Figure 19. Optical thickness comparison. Shot #13 is a standard value, while #40, #41, #42 and #91 are outliers.

In Figure 19, the average value of the optical thickness is plotted as a reference for comparing individual images. Shots #40, #41, #42 and #91 have some values at the center of the spray that are three times higher than the average. The rest of the shots show similar behavior to shot #13. Therefore, it was clear that some additional factors affected these four shots; so, they were discarded.

4.3 INVERSE ABEL TRANSFORM

After the data was accurately ensemble averaged, the next step was to transform the line-of-sight data into a planar measurement along the spray centerline. This section assesses the accuracy of using the Inverse Abel Transform on different types of data relevant to diesel spray mixing. The algorithm used was the one implemented by Muhammad Firman Kasim (University of Oxford, 2016) [37] in Matlab. This methodology was based on the three-points method described in reference [38].

4.3.1 TESTING SYNTHETIC DATA

First, to test the behavior of the algorithm, we tried some simple analytic functions, of which the inverse results are already known from reference [39]. The first trial function used was:

$$F(y) = 2\sqrt{a^2 - y^2} \quad \text{Equation 11}$$

In Equation 11, a is a parameter, which was chosen equal to 2, and y is the vertical axis variable. The inverse Abel transform of Equation 7 is the rectangle function Π_a :

$$f(r) = \Pi_a(r) = \begin{cases} 1 & 0 < r < a \\ 0 & \text{otherwise} \end{cases} \quad \text{Equation 12}$$

In the next figure, the original function $F(y)$ (Equation 11) is plotted on top. On the bottom is plotted the inverse Abel transform calculated with Matlab in addition to the expected analytical result (Equation 12). The value of a was chosen equal to 2.

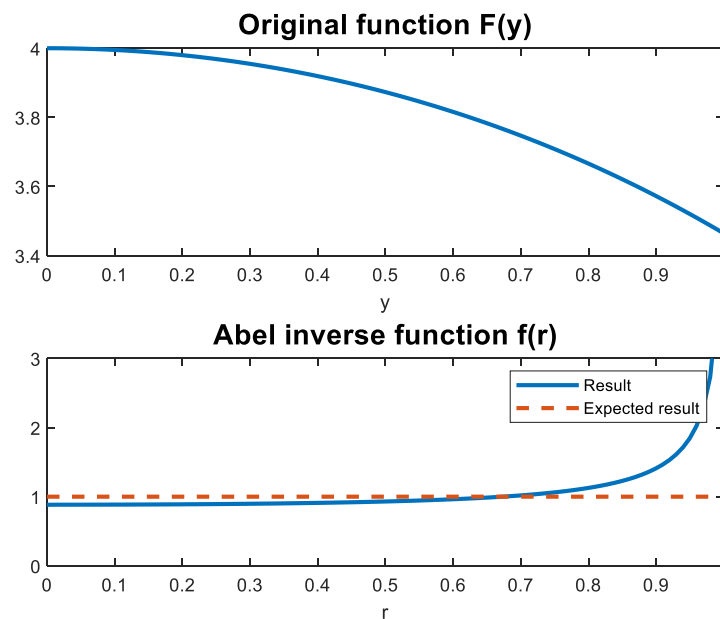


Figure 20. Inverse Abel transform test of a simple analytic function (Equation 11)

In Figure 20, it can be observed that the inverse Abel transform gives us a result similar to the expected but with a noticeable error. However, this error becomes significantly larger

around $r=0.9$, where the inverse Abel transform result should remain at 1. Therefore, for these type of functions, other methods should be considered.

The second function tested was:

$$F(y) = a - y \tag{Equation 13}$$

Its inverse Abel transform function is:

$$\frac{1}{\pi} \cosh^{-1} \left(\frac{a}{r} \right) \tag{Equation 14}$$

The results are plotted below in the same format.

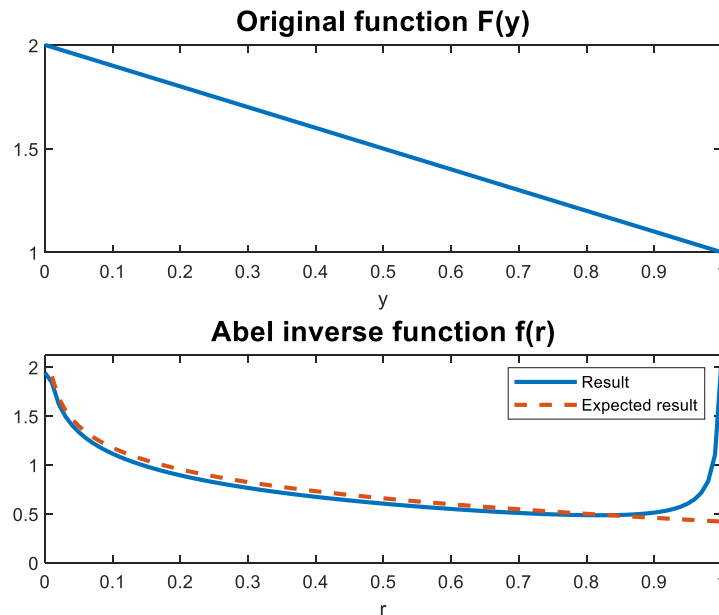


Figure 21. Inverse Abel transform test of a simple analytical Equation 13

Here, once again, we observe that the result is close to the expected one, but there is still an error all through the function, which becomes noticeably larger at large values of r .

To check the cause of this error, we evaluate the same functions but with different parameters that make the functions go to zero when $y=1$. The results of this evaluation can be seen in Figure 22.

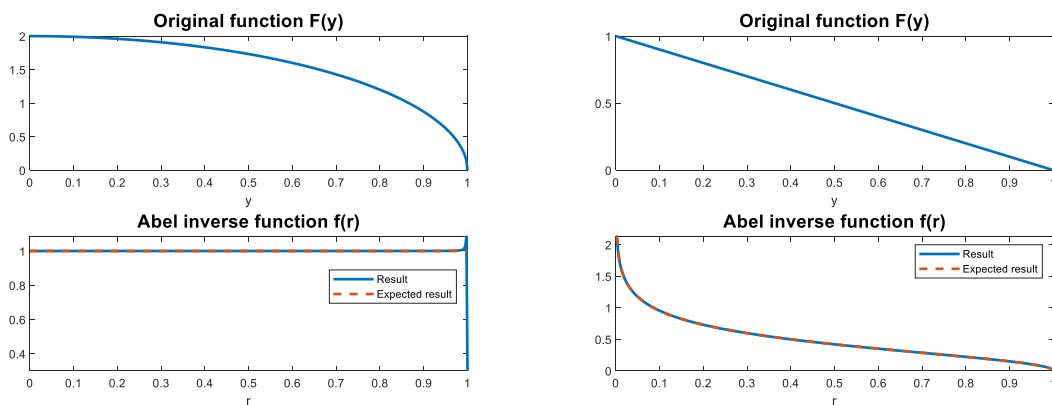


Figure 22. Inverse Abel transform for Equation 11 and Equation 13 with $a=1$.

Now we can see that both functions are correctly converted by the inverse Abel transform. From this analysis we can extract that it is crucial that the input function of the transform decays to zero; this will guarantee much better performance. However, for the first function (Equation 11), there is still a small error at $r=1$; nevertheless, much smaller than on the previous evaluation.

Therefore, using a function that decays to zero is crucial for a good performance of the inverse Abel transform; however, this does not ensure a perfect result for all the functions.

However, the projected density data that we used has a Gaussian shape through the radial axis (Figure 23), which decays to zero at the edges of the spray. For this reason, a good performance of the transform was expected, so our next step was to check its performance on a Gaussian curve. Further analysis of the distribution and statistical parameters of our data is analyzed in the next chapter.

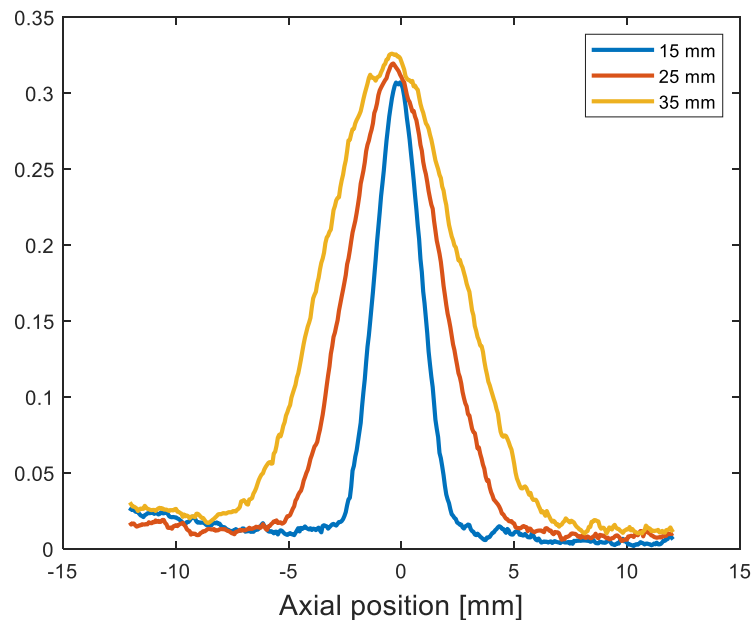


Figure 23. Radial plot optical thickness at 15, 25 and 35mm from the nozzle. Experimental conditions: 900K, 22.8 kg/m³, 1000 bar injection pressure. 3.5ms

To check the behavior of a Gaussian curve, the analytic development of the inverse Abel transform for a gaussian function was performed. The equation of a Gaussian is shown below.

$$F(y) = \frac{1}{\sigma\sqrt{2\pi}} e^{-\frac{(y-\mu)^2}{2\sigma^2}} \quad \text{Equation 15}$$

In Equation 15, σ is the variance and μ the mean. If we assume that the z-axis is placed on the centerline of the spray, the value of μ is zero. Furthermore, assuming $\mu=0$ makes it simpler to develop the analytical expression.

To calculate the inverse Abel transform analytically, the derivative of the function $F(y)$ is needed. The derivative of the gaussian for the case $\mu=0$ is the following.

$$\frac{dF(y)}{dy} = -\frac{y}{\sigma^3\sqrt{2\pi}} e^{-\frac{y^2}{2\sigma^2}} \quad \text{Equation 16}$$

Then the inverse Abel transform is calculated following Equation 7, the result is shown in Equation 18.

$$f(r) = -\frac{1}{\pi} \int_r^1 -\frac{y}{\sigma^3\sqrt{2\pi}} e^{-\frac{y^2}{2\sigma^2}} \frac{1}{\sqrt{y^2 - r^2}} dy \quad \text{Equation 17}$$

$$f(r) = -\frac{\text{erf}\left(\frac{-\sqrt{1-r^2}}{\sigma\sqrt{2}}\right)}{2\pi\sigma^2} e^{-\frac{r^2}{2\sigma^2}} \quad \text{Equation 18}$$

In Figure 24, the inverse Abel transform is shown for $\sigma = 0.2$.

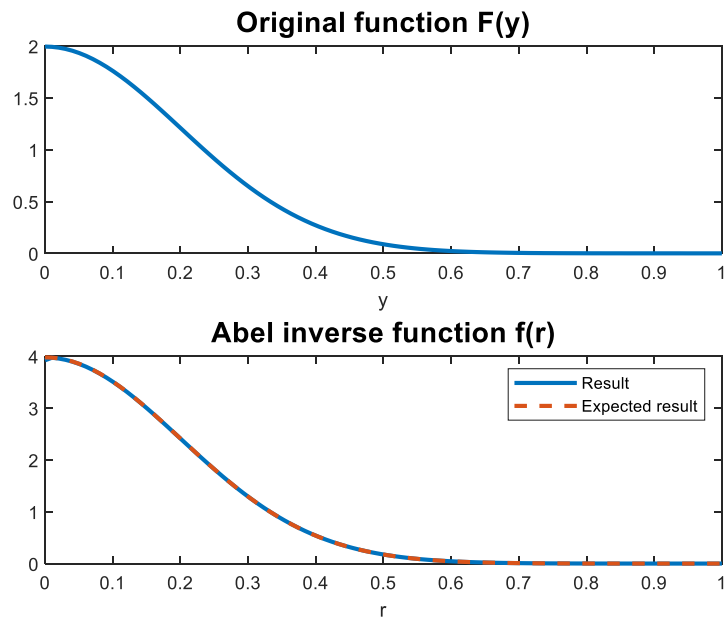


Figure 24. Inverse Abel transform for a Gaussian function

We observe that in the case of a Gaussian function, the algorithm provides an excellent match with the analytically calculated plot. Therefore, this algorithm was selected for use with our data due to its gaussian behavior. However, there is a small error $r=0$, less than 2%; nevertheless, this can be important depending on the application.

This error can be reduced by increasing the number of points used for the calculation, in other words, increasing the resolution. To prove this, we tested the inverse Abel transform with different y resolutions: 100, 200 and 400 points for the range $y=0$ to $y=1$, the results are plotted in Figure 25.

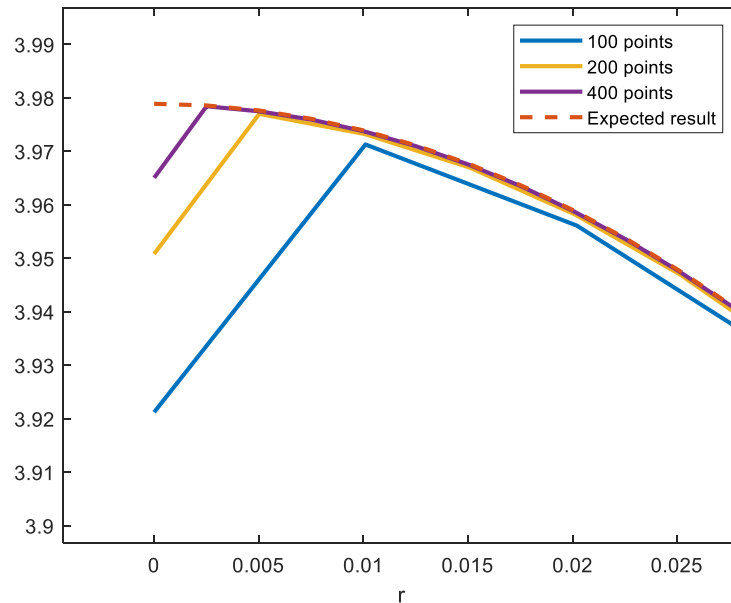


Figure 25. Inverse Abel transform error comparison for different resolutions. Gaussian function

From this plot, it is clear that resolution affects the performance of the inverse Abel transform. The error for the first point of the plot varies from almost 2% to less than 1%. Furthermore, if we do not have enough points to represent the Gaussian function, the function can result in a sharp drop at the centerline of the planar transform. Then, if this sharp drop occurs for an inverse Abel transform result, 2 and 4 times increase in the resolution must be analyzed to remove this undesired effect.

4.3.2 EVALUATION OF INVERSE ABEL TRANSFORM ON ECN PLANAR SPRAY

MIXING DATA

After the performance of the inverse Abel transform for Gaussian functions was proved, the transform was evaluated for an existing planar spray mixing measurement in the literature. The data used for this test was retrieved from the ECN website [40], which provides sets of data for different temperatures, pressures and densities. We selected a Spray A data set that had the same conditions of our experiment: 900 K temperature, 22.8 kg/m³ density, 100 MPa injection pressure, and an axially drilled single orifice injector with a nominal orifice diameter of 90 μm. The planar measurement was converted to a projected fuel planar measurement by performing a revolution of the data about the centerline first and then integrating it about the line-of-sight, the result is shown in Figure 26.

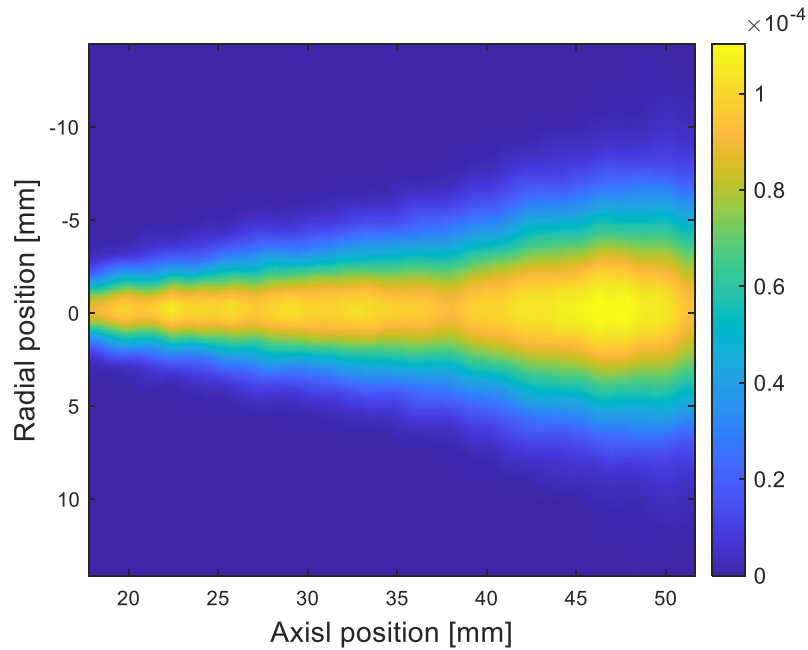


Figure 26. Projected fuel concentration of Spray A based on the integration of existing planar Rayleigh scattering measurements. [kmol/m^2] Experimental conditions: 900 K, 22,8 kg/m^3 , 1000 bar injection pressure.

After, the inverse Abel transform was applied to Figure 26 to obtain the reconstructed planar concentration. The result was compared with the original measured planar fuel concentration (Figure 27).

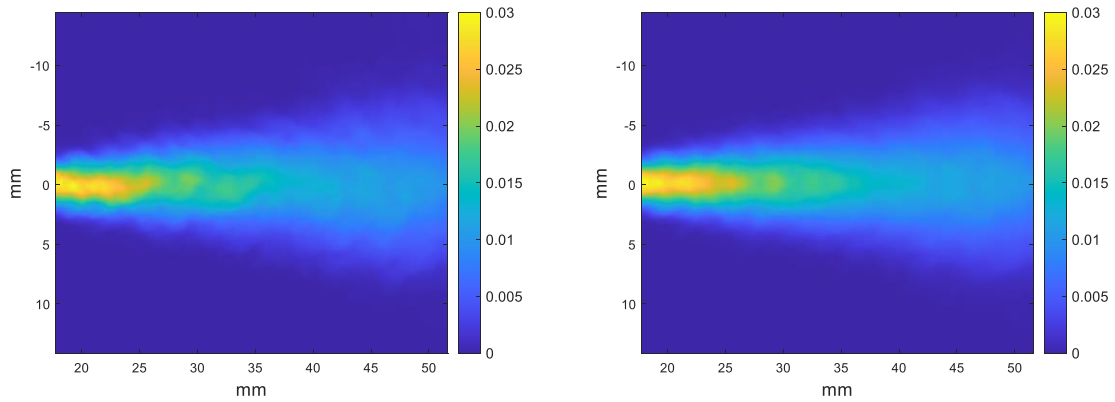


Figure 27. Measured planar fuel concentration(left) and Abel reconstruction of planar fuel concentration from line-of-sight integrated projected fuel concentration(right).[kmol/m^3] Experimental conditions: 900 K, 22,8 kg/m^3 , 1000 bar injection pressure.

We can observe that the result obtained by the inverse Abel transform matches with the overall behavior shown by the ECN data. However, some of the asymmetries and particularities are not captured by the inverse Abel transform. To better compare the results, additional plots were prepared. An important plot that is often used is the centerline planar fuel concentration; this is shown in Figure 28.

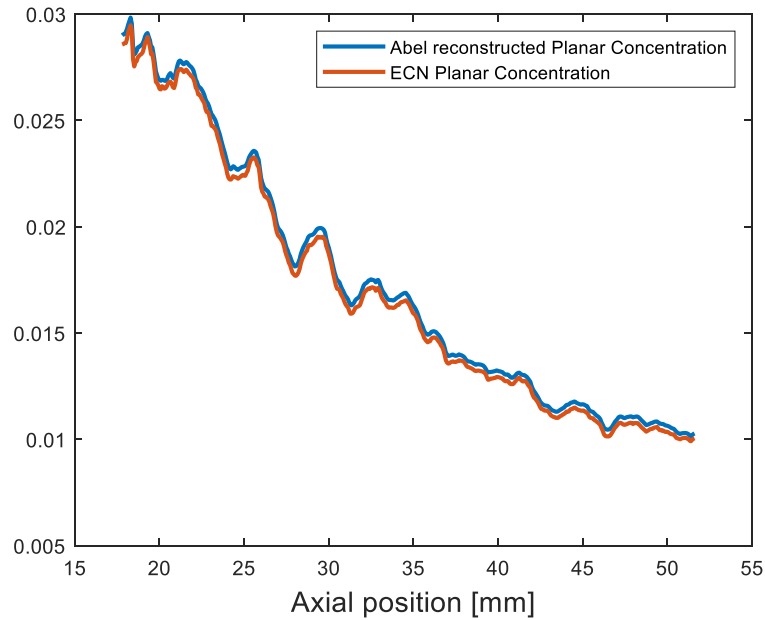


Figure 28. Comparison of measured planar fuel concentration and Abel reconstructed planar fuel concentration along the spray centerline of Spray A [kmol/m³] Experimental conditions: 900 K, 22,8 kg/m³, 1000 bar injection pressure.

The difference between the real planar fuel concentration and the planar fuel concentration obtained by the inverse Abel transform is low and consistent all through the plot. In this case, the Abel transform result is higher than the real value. The reason for this is that the maximum value for the spray is not always at the centerline, while for the inverse Abel transform it is at the center due to its approach. This can be better observed at a radial plot for a fixed axial position, Figure 29.

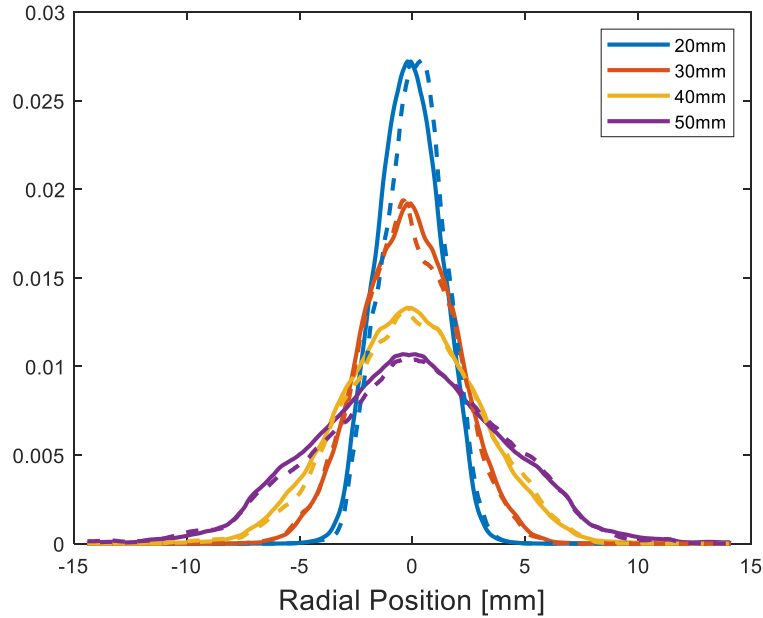


Figure 29. Radial plot comparison between Abel reconstructed planar fuel concentration (solid line) and measured planar fuel concentration in Spray A (dashed line) at 20, 30, 40 and 50 mm from the nozzle.

[kmol/m^3]

In Figure 29, we can observe the difference in the maximum planar fuel concentration location between the ECN data and the reconstructed profile. Also, we can observe that the profile evolves from a Gaussian curve to a triangular shape far downstream of the injector nozzle. However, the performance of the inverse Abel transform is still good and close to the real result.

The overall conclusion we can extract from this testing is that the Abel transform outputs valuable results, especially for Gaussian functions, because as we have demonstrated the inverse Abel transform of a Gaussian function is another Gaussian function multiplied by a

factor. However, triangular-shaped functions can also be transformed with a usable result. On the other hand, some more complex functions with particularities can be challenging for this method. Therefore, we used Gaussian fits for our raw data prior to performing the Inverse Abel Transform. Also, if a sharp drop at the centerline of the planar transform resolution is found, a 2 and 4 times in resolution must be analyzed to reduce this possible source of error.

Chapter 5. RESULTS

In this chapter, the inverse Abel transform was applied to the collected data following the procedure explained in the methodology section. First of all, an analysis of the data was performed to determine how many injections were necessary to calculate a relevant ensemble average. Then, using the number of injections selected, the planar fuel concentration was calculated and evaluated against ECN Rayleigh data.

5.1 DETERMINING A STATISTICALLY RELEVANT ENSEMBLE AVERAGE

The objective of this analysis was to obtain an accurate ensemble average of the flow field. As we have seen in the previous chapter, an accurate inverse Abel transform relies on a smooth input function; therefore, the signal noise in a typical single-shot image would produce significant non-physical fluctuations in the transform. In order to verify that the data taken was representative of the spray behavior, several checks were performed. First, the standard deviation of the optical thickness was calculated and examined. Second, Lilliefors test was performed prior to calculating the confidence interval for the ensemble average. Finally, synthesizing this information, the number of shots necessary for this type of measurements was verified.

5.1.1 STANDARD DEVIATION

When experiments are performed there are always some errors/uncertainty associated with the measures. The error is a combination of variations due to the phenomenon to study and additional interfering factors. Then, by taking multiple observations and averaging them, we can identify the variations due to the phenomenon if the error is normally distributed. The spread of the data can be measured by a variance estimator, such as the standard deviation. When sampling, it is important to ensure that the observations are independent; for this purpose, random samples are used.

To estimate the variance, we used the standard deviation, which was calculated as:

$$s = \sqrt{\frac{\sum_{i=1}^n (x_i - \bar{x})^2}{n - 1}} \quad \text{Equation 19}$$

In Equation 19, s is the standard deviation, x_i sample value, \bar{x} the mean and n the number of samples. The denominator used was $n-1$ instead of n , for normalizing the sample standard deviation.

To investigate how the standard deviation varies as we included more injections in the analysis, we studied the standard deviation of the ensemble-averaged optical thickness in several regions. Examining the standard deviation of a single point can result in inaccurate conclusions; instead, we decided to evaluate it in small boxes of adjacent pixels. The selected region must be small enough so that the selected points have similar values, but large enough to provide an average trend.

Regions at the edges of the spray are more sensitive to background noise due to the lower concentration at those points, but regions at the centerline have a higher concentration, so they are less sensitive to it. Therefore, in order to study the oscillations in the concentration of the spray, the centerline is more suitable because its variance is predominantly represented by the spray fluctuations rather than background noise. For these reasons, we calculated the standard deviation of the optical thickness for boxes of 10x20 pixels at different locations of the centerline.

As the 100 injections events (96 with the outliers removed) were taken in two sets of 50 injections, we perform the same analysis for the two sets separately. The procedure was to calculate the standard deviation of the selected region using from only 2 ensemble-averaged randomly selected injections to 47 ensemble-averaged injections for the first set and 49 for the second. Then the resulting standard deviation was plotted against the number of shots used in the ensemble average. In Figure 30, we plotted the results for the two sets at two locations: the first box of pixels was situated 20mm downstream at the centerline, and the second one 30mm downstream also at the centerline.

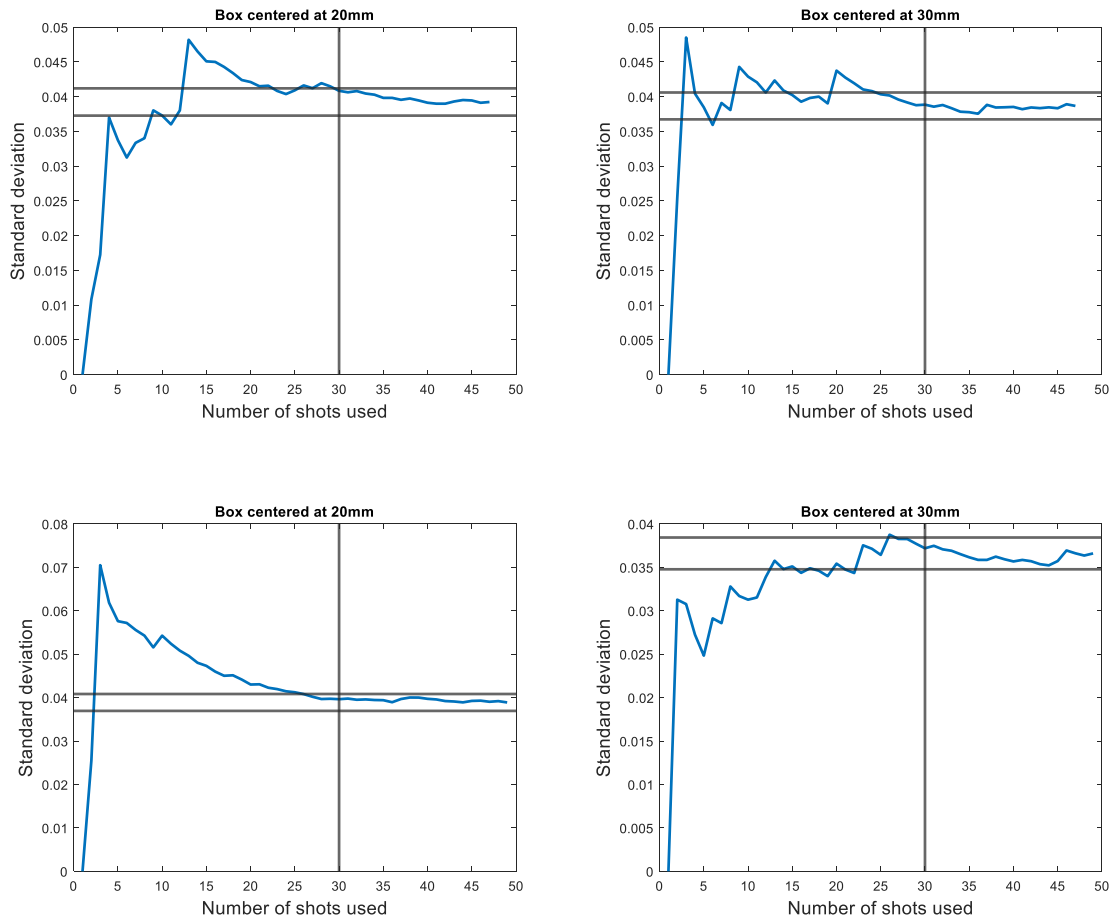


Figure 30. Standard deviation vs Number of shots used without the outliers. Two top plots are for the first set of 47 injections; two bottom plots are for the second set of 49 injections. Locations: centerline at 20 and 30 mm downstream of the injector nozzle. Time: 3.5ms

In Figure 30, the standard deviation of ensemble-averaged optical thickness can be observed for two positions and the two sets. Besides, two horizontal lines were plotted at a $\pm 5\%$ of the final value; also, a vertical line at 30 shots was included. It is clear that as the number of shots is increased; the standard deviation tends to stabilize. When the number of shots used is low, the standard deviation changes significantly depending on how similar the selected

shots used are. On the contrary, when the number of shots used is over thirty, the changes in the standard deviation are low. This plot was done on additional positions and instants of time, obtaining similar results. Therefore, to have a data set with a standard deviation that contains all the inherent variations of the spray due to its turbulent behavior, we needed 30-40 shots in the ensemble average mixing measurement.

5.1.2 CONFIDENCE INTERVAL

In addition to the variance, there is another statistical parameter that measures the accuracy of how precise the sample represents the population, this is the standard error. The standard error of a population, s_x , can be calculated as the following.

$$s_x = \frac{s}{\sqrt{n}} \quad \text{Equation 20}$$

Every measure taken experimentally has an associated uncertainty; for this reason, confidence intervals are used. If a measurement follows a normal distribution and the observations are independent, then the error in the sample average normalized follows a t-distribution.

It is often assumed that the distribution of an experimental case follows a normal distribution. However, it was decided to test if this was the case if we use 40 injections using the Lilliefors test. This test estimates the mean and standard deviation of the population to normalize the sample variance. Then the test is computed by finding the maximum discrepancy between the empirical distribution function and the cumulative distribution function, more

information about the Lilliefors test can be found at reference [41]. The null hypothesis was that the data comes from a normal distribution; the alternative was that it does not come from such a distribution. This test was performed at a 5% significance level using Matlab function ‘lillietest’.

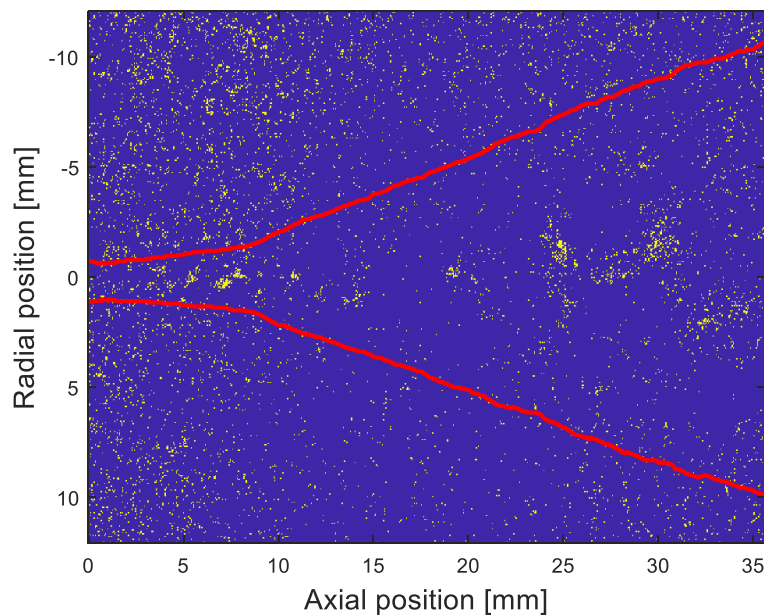


Figure 31. Lilliefors test for 40 raw images at 3.5ms. Yellow dots represent rejecting the null hypothesis.

Blue dots represent not rejecting the null hypothesis. Edge of the spray is represented in red.

In Figure 31, it is observed how most of the points of the spray are represented in blue, which means that at a 5% significance level we can say those points come from a normal distribution. However, there are a minority of points of the spray where we cannot assure that they come from a normal distribution at a 5% significant level because of the highly turbulent behavior of the spray. However, the number of points where we can assure that the

error comes from a normal distribution is higher than the points were, we cannot. Moreover, the central limit theorem states that as the sample size becomes larger the distribution approximates a Gaussian curve. Therefore, we continued developing our confidence interval analysis using the assumption of the normal distribution for the statistical calculation on the spray region.

The t-distribution, $t_{n-1;\alpha/2}$, depends on two parameters, the degrees of freedom, n , and the level of probability, $1 - \alpha$. Then, the confidence interval for the mean can be calculated using the t-distribution and the standard error with the following expression.

$$\bar{x} \pm t_{n-1;\alpha/2} \cdot S_{\bar{x}} \qquad \text{Equation 21}$$

The confidence interval for the ensemble average was calculated using a 95% probability level. It was calculated using a different number of shots each time to validate the number of shots necessary to have a representative mean.

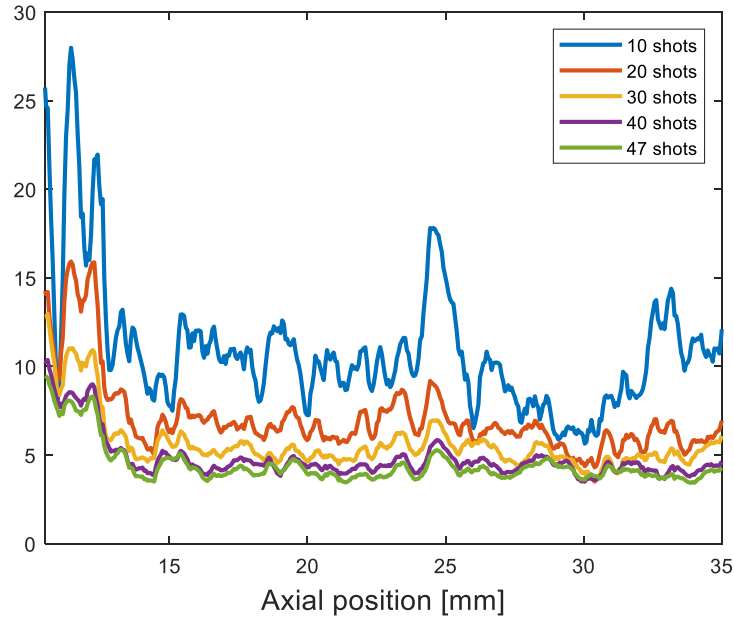


Figure 32. Confidence interval (%), $t_{n-1;\alpha/2} \cdot S_{\bar{x}}$, at the centerline, using different number of shots.

In Figure 32, the confidence interval is presented as a percentage of the average value. It is clear that as we increase the number of shots used, the confidence interval is going to become smaller, as it can be inferred from Equation 20. Nevertheless, the number of shots that can be taken is limited. Consequently, a balance between the number of shots taken and the desired confidence interval must be reached. Previously, we saw that 30-40 shots converge on a nearly constant variance in the measurement of optical thickness along the centerline of a spray.

Regarding Figure 32, it is clear that 10 shots are not enough because the confidence interval was consistently over 10% and almost reached 20% at some points; however, 30 shots gave us a confidence interval consistently around 6%. Additionally, more than 40 shots reduced

the confidence interval, but not in a significant way to justify the extra shots. Every extra measurement in these types of experiments is extremely costly not only economically but in terms of time and labor. Hence, for this type of measurements, 30 to 40 shots gave us a reasonable confidence interval for the ensemble average while maintaining the time and cost of the experiment low. This result matches with the conclusion of the previous test and analysis of these chapters. Therefore, we decided to use 40 shots for our experiment.

5.2 INVERSE ABEL TRANSFORM APPLIED TO THE UV-VIS DBI

DATA

To perform the inverse Abel transform to our data, we began with the optical thickness. First of all, we observed that the spray had an offset angle from the centerline. This must be addressed before performing the inverse Abel transform; otherwise, the centerline of the spray could not be identified correctly, which would result in an inaccurate inverse Abel transform.

5.2.1 CORRECTING FOR SPRAY POINTING ANGLE

Due to the highly turbulent behavior of the spray, the maximum optical thickness did not always occur at the centerline. These fluctuations were reduced when the ensemble average was performed; however, a pattern was discovered. To identify the offset angle of the spray

we plotted the radial position at which the maximum optical thickness occurs for each axial position. Although the maximum value is not necessarily always at the same point, the trend should remain stable and horizontal for a centered spray.

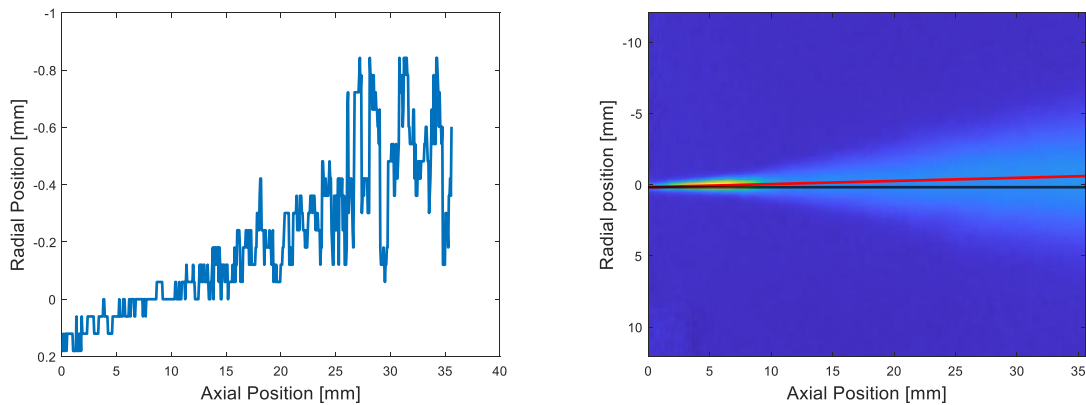


Figure 33. Left image: radial position of the maximum value of measured optical thickness as a function of the axial position from the injector nozzle exit. Right image: pointing angle of the spray (red) vs horizontal line (black) for optical thickness at 3.5ms

However, in Figure 33 it is clear that there is a shift in the maximum values in the negative radial direction with increasing distance downstream of the injector nozzle., which indicates that the spray is pointing at an angle from the horizontal axis of the injector nozzle. The position of the maximum goes to the negative values of the radial axis. So, according to the placement of our axis for optical thickness, the spray is pointing upwards. To correct this spray pointing angle, we rotated the image clockwise. The offset angle was determined through Figure 33 by trigonometry. A linear fitting was used to obtain the slope of the overall trend. Then the angle was calculated, resulting in 1.2°.

Once the offset angle is known, the ensemble average optical thickness was rotated to compensate it. The command used to perform the rotation was 'imrotate'. A final check was done to verify that the trend remained horizontal after this correction.

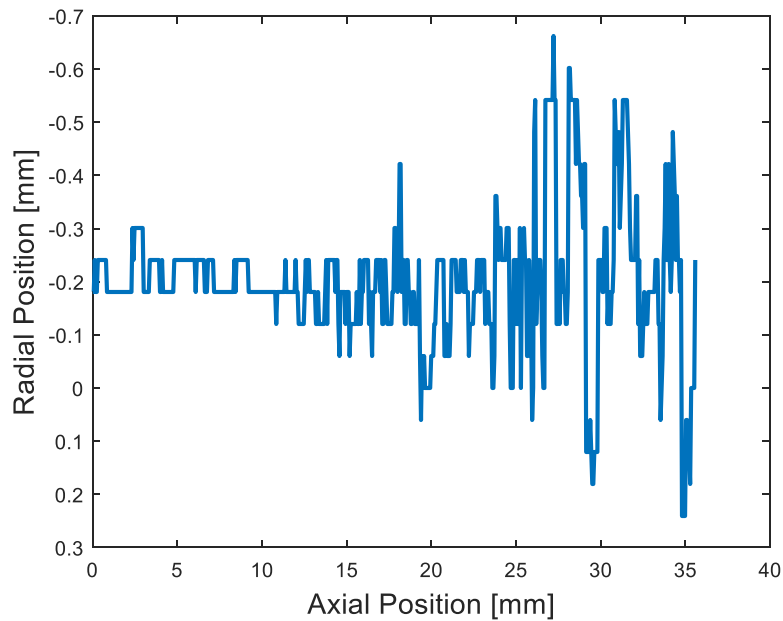


Figure 34. Position of the maximum value for the rotated optical thickness.

5.2.2 GAUSSIAN FIT

Next, although we have seen that the inverse Abel transform can work with other functions different from a gaussian curve, we decided to use a gaussian fit to our projected density data. The reasons are that the inverse Abel transform performs better with a gaussian curve, we could increase the resolution of the y-axis by evaluating the Gaussian curve between our data points, and for a 3D or slice representation, the final image would be much cleaner and

higher quality. At the same time, the Gaussian fit helps to reduce the possible noise that could be present in the signal.

The gaussian fitting was done at each axial position; an example is shown in Figure 35.

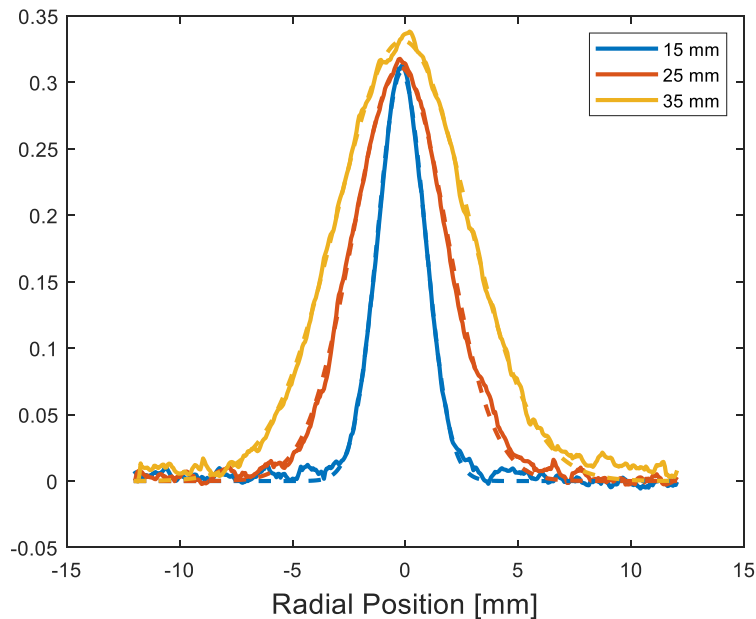


Figure 35. Gaussian fit optical thickness at 15, 25 and 35 mm from the nozzle. The solid line is the optical thickness, and the dashed line is the Gaussian fit.

It can be observed in Figure 35 that the optical thickness has gaussian behavior on the radial axis. The Gaussian fit matches accurately all through the spray, from the near region to the fairest one. The greatest difference between the optical thickness and its gaussian fit is at the edges of the spray, where the noise is higher.

Before performing the inverse Abel transform to our data, we decided to take some additional points for the gaussian curve. As the Gaussian curve has an analytical expression,

every point at the x-axis has an $f(x)$ value that can be calculated. Our radial range remained the same: from -12.04 to 12.04 mm, however instead of using 401 points on the vertical axis, we used 6401.

When we used the 401 points data, the Gaussian curve did not have enough resolution to capture the curvature of the function. As a result, the inverse Abel transform was outputting some results that were not what was expected. As it was explained before, resolution is a key aspect that can influence the transform, especially at the centerline. In Figure 36, it can be observed how the inverse Abel transform of the 400 points has a sharp decay at the center of the spray, while the 1600 inverse Abel transform follows a Gaussian curve.

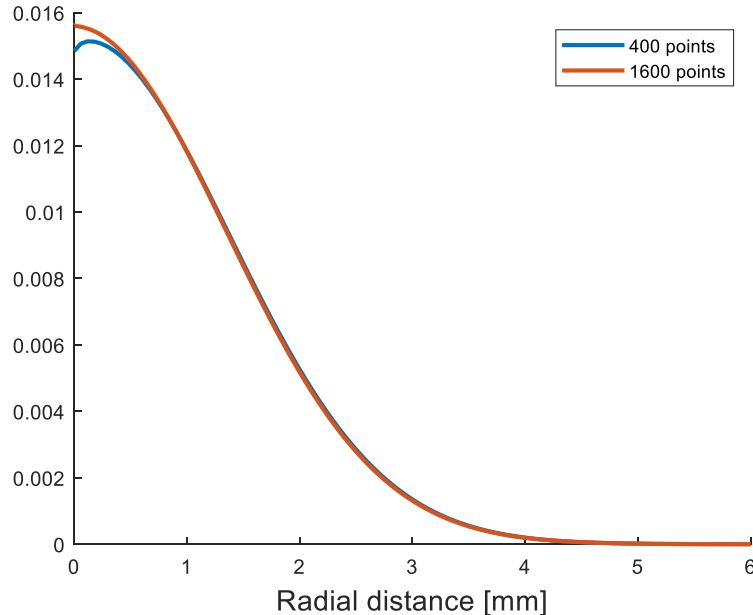


Figure 36. Inverse Abel transform of projected fuel concentration comparison between 400 and 1600 data points at 18 mm downstream. Planar fuel concentration [kmol/m³]

Then, when the resolution was increased, the curvature of the gaussian was much better modelled, which helped the inverse Abel transform to output a more consistent result. Then, once the ensemble average of the optical thickness was rotated and fitted Gaussian curves, the projected fuel concentration was calculated following Equation 10. In Figure 36, the inverse Abel transform of the projected fuel concentration is plotted; in other words, the planar fuel concentration.

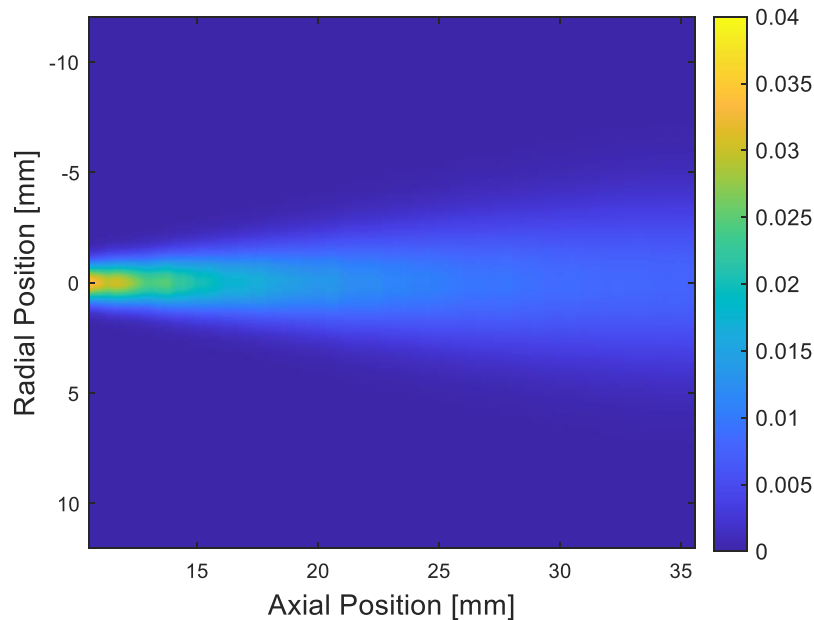


Figure 37. Planar fuel concentration obtained by the inverse Abel transform of the line-of-sight measurement of projected fuel concentration. [kmol/m³]

In Figure 37, the planar fuel concentration along the centerline of the spray can be observed. It is a smooth image without noise, thanks to the use of gaussian functions. To compare and validate the results, an ECN data set was used.

Indeed, the ECN data set used was the same that was previously employed to test the inverse Abel transform, because the experimental conditions were the same. The comparison made was done for the centerline of the planar concentration, and for the radial planar concentration.

First, the planar concentration for the centerline of the spray was plotted in Figure 38. The ECN data and our UV-VIS data had different ranges on both the axial and radial axis. For this first plot, only the axial axis is relevant, because we are comparing the planar concentration just for the centerline of the radial axis. The axial axis was adjusted to only plot the range where we had data for both sets.

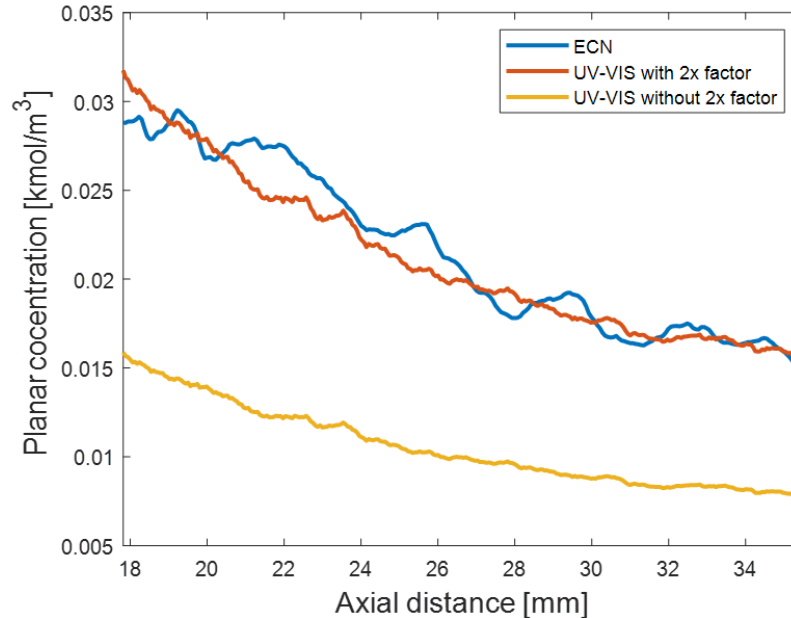


Figure 38. Validation of the predicted planar fuel concentration along the spray centerline using and inverse Abel transform against ECN Spray A planar Rayleigh scattering measurement.

In Figure 38, the planar concentration for the UV-VIS data was multiplied by a two times factor. Although there is uncertainty in the source of this data offset, we hypothesize that this offset could be due to a pressure dependence of the naphthalene absorption coefficient. There is no existing literature data for naphthalene absorption coefficients at the pressures used in these measurements, but other isomers of naphthalene demonstrate pressure dependencies in this range. [34] [35] This phenomenon is planned to be evaluated in the future by our research group to make the data quantitative. For this project, the adjustment factor for this phenomenon was selected to be equal to 2.

Then, when the planar concentration plot for the centerline is compared, it can be observed that the overall concentration matches with the ECN data. It can be observed how the concentration decays as we get further from the nozzle. This is an important factor for the comparison because the trend or decay does not depend on the pressure dependence issue, yet to be evaluated. Additionally, radial plots were compared to confirm this agreement between the two diagnostics, Figure 39.

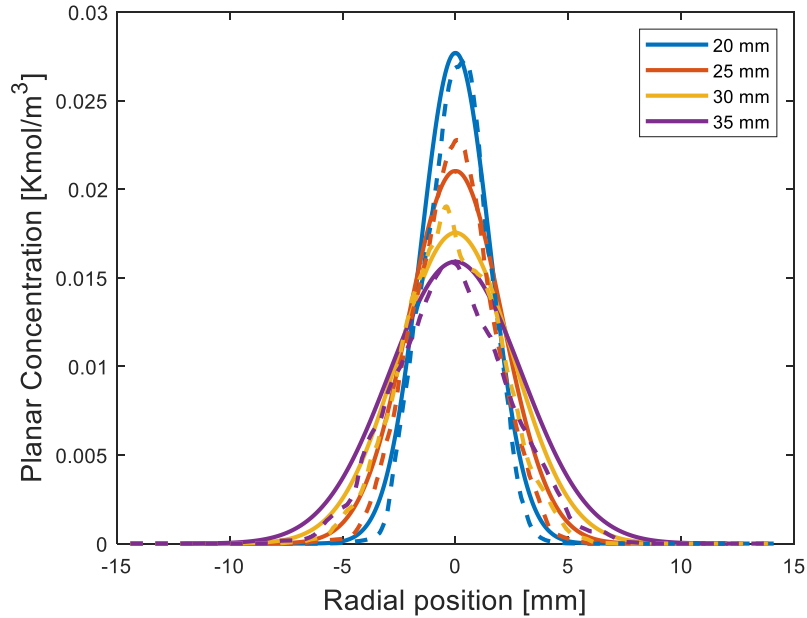


Figure 39. Planar fuel concentration at 20, 25, 30 and 35 mm from the nozzle. The solid line is the UV-VIS result, and the dashed line is the ECN data.

Again, the data was multiplied by 2x, consistent with the multiplication factor necessary to align the two data sets along the spray centerline. It is observed that the ECN data has a closer gaussian behavior upstream, while further downstream the shape evolves into a more triangular curve. However, the UV-VIS results are gaussian for the whole spray, which makes the highest difference between the two diagnostics to occur further downstream. Additionally, asymmetries and non-gaussian behaviors cannot be replicated by the inverse Abel transform method.

Nonetheless, the overall match between the two diagnostics is clear for both the centerline (Figure 38) and the radial plot (Figure 39). These results can be promising once the pressure

dependence issue is addressed. The next step was to check the uncertainty introduced by the inverse Abel transform.

5.2.3 UNCERTAINTY ANALYSIS

There are many types of uncertainty that can be analyzed, such as the one produced by how the data is fitted. However, in this project, we want to understand how uncertainty in the mean fuel concentration is propagated through the inverse Abel transform. Additional sources of uncertainty of this data were analyzed by C. Godbold [32].

To measure the propagation of uncertainty in the mean fuel concentration, the standard deviation was used. As explained in the methodology chapter, the projected fuel concentration was determined after the optical thickness was rotated and fitted with a Gaussian. The projected fuel concentration was then calculated by dividing the optical thickness by the absorption coefficient and the naphthalene concentration, as shown in Equation 10. Therefore, optical thickness and projected fuel concentration are directly proportional, which means that we could analyze the uncertainty of the optical thickness and translate it for projected fuel concentration.

First, the standard deviation of the optical thickness was added and subtracted for each pixel, to create the upper and lower boundaries, respectively. Second, these boundaries were then rotated the offset angle calculated in 5.2.1. Third, the boundaries were fitted into Gaussian curves, following the same procedure described before.

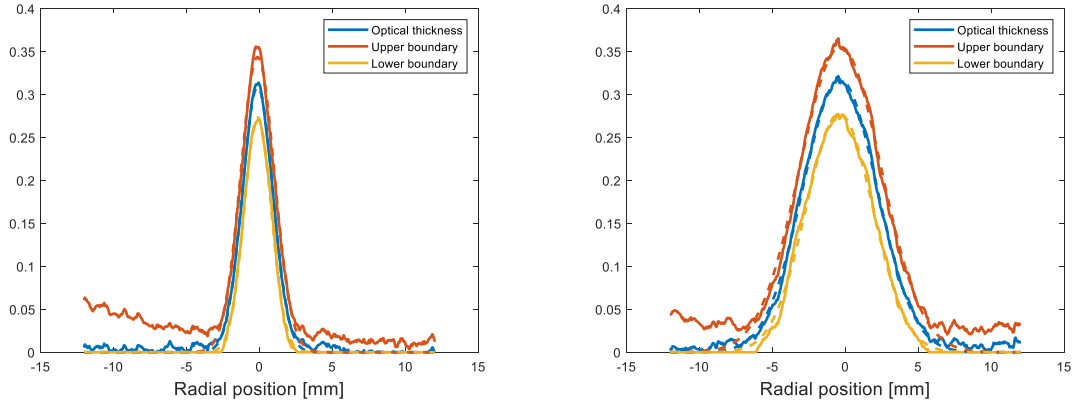


Figure 40. Radial plot of optical thickness plus estimate of the upper and lower bound in the mean optical thickness at 15 (left) and 30 mm (right) from the nozzle. The solid line is the measured optical thickness, and the dashed line is the gaussian fitted curve. Number of measurements used: 40

In Figure 40, two radial plots are displayed for two axial positions. The results for the rest of the spray are similar and consistent with the two examples shown above. It can be observed that for the upper bound of uncertainty in the mean optical thickness, the edges of the optical thickness do not go to zero, due to the added standard deviation. However, the gaussian does asymptotically approach zero at the edges due to its definition. On the other hand, when we subtract the standard deviation to the optical thickness, negative values are reached. In this case, it was decided to correct these values prior to the gaussian fit in order to reduce the complexity of the fitting. Every negative value of the lower boundary was changed to zero. Then, the Gaussian was fitted. As it can be observed in Figure 40, the fitting for both upper and lower boundaries is accurate and matches well the data.

The next step was to perform the inverse Abel transform for the upper and lower bounds of uncertainty. The same procedure described in the previous section was used. First, the radial resolution was resampled to a higher resolution of 6400 y data points, and then the inverse Abel transform is applied for every axial position. In Figure 41, an analysis of the inverse Abel transform was performed for a single axial position, to see in more detail its behavior.

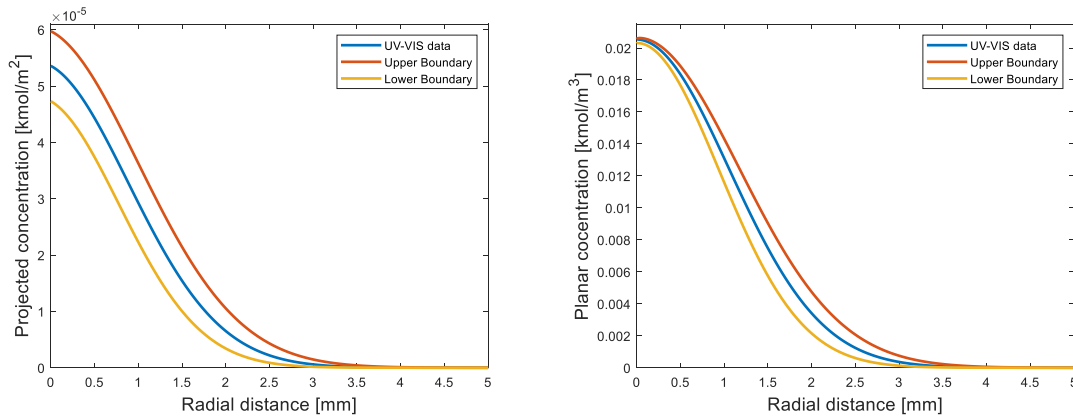


Figure 41. Input and output of the inverse Abel transform for the UV-VIS DBI data and its boundaries at 15mm downstream of the injector nozzle.

On the left, the input of the inverse Abel transform is plotted. It can be observed that the upper and lower uncertainty bounds are offset the same distance from the mean data, due to the standard deviation applied. Though, the inverse Abel transform does not conserve the equivalent upper and lower uncertainty offset from the mean for the output shown on the right. Instead of outputting three identical curves with an offset, the results are three different curves with a small offset. Therefore, for these type of cases, the greatest difference between the mean measurement is not at the centerline but where the measured optical thickness

approaches the noise floor; while at the edges of the spray falls back to zero as expected.

This behavior changes depending on the axial position, there were other cases in which the output resulted in three similar curves with a constant offset all through the spray, like the example shown in Figure 42.

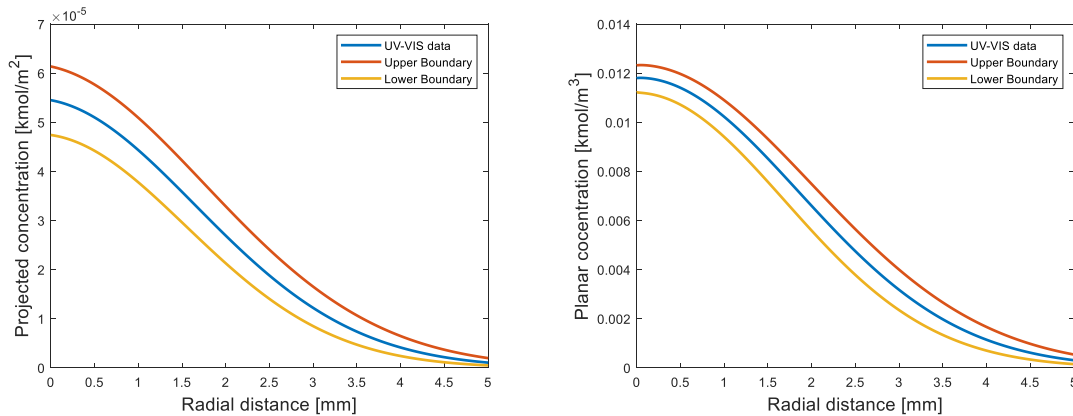


Figure 42. Input and output of the inverse Abel transform for the UV-Vis DBI data and its boundaries at 23.4 mm

In Figure 42, contrary to Figure 41, we observed that an offset is maintained from the input to the output of the inverse Abel transform, with much more similar curves between the mean and its upper and lower uncertainty bounds. However, this was not the most common case through the spray. The general trend as we move downstream in the spray can be observed in Figure 43.

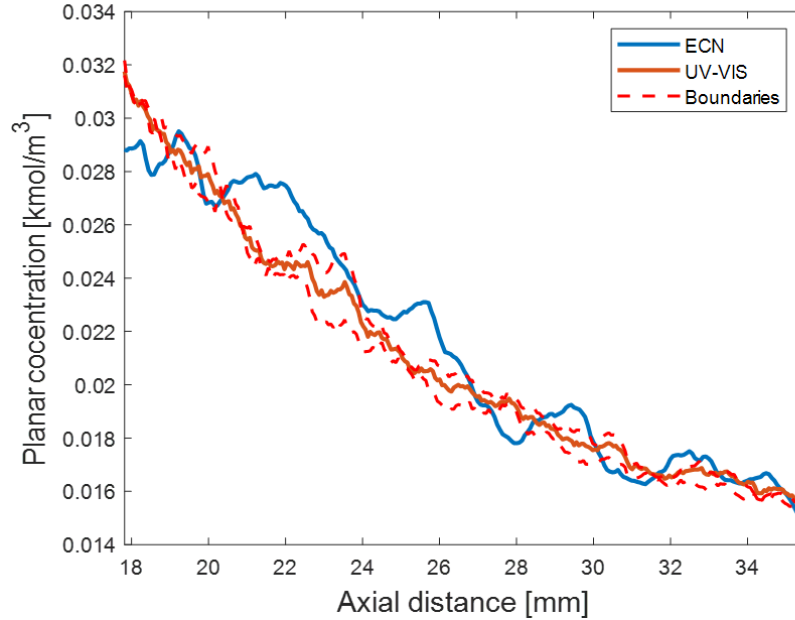


Figure 43. Centerline planar fuel concentration comparison between ECN planar Rayleigh measurements and inverse Abel transform of UV-Vis DBI.

In Figure 43, it can be observed that the uncertainty introduced by the inverse Abel transform is low in comparison to the mean planar fuel concentration. In this plot, both cases described in Figure 41 and Figure 42 can be noticed all through the centerline. At some point, the uncertainty in the mean planar fuel concentration can be as low as 1% while at other it reaches a 6% difference. This variation is due to the high sensitivity the inverse Abel transform is subjected to the fluctuations in the input.

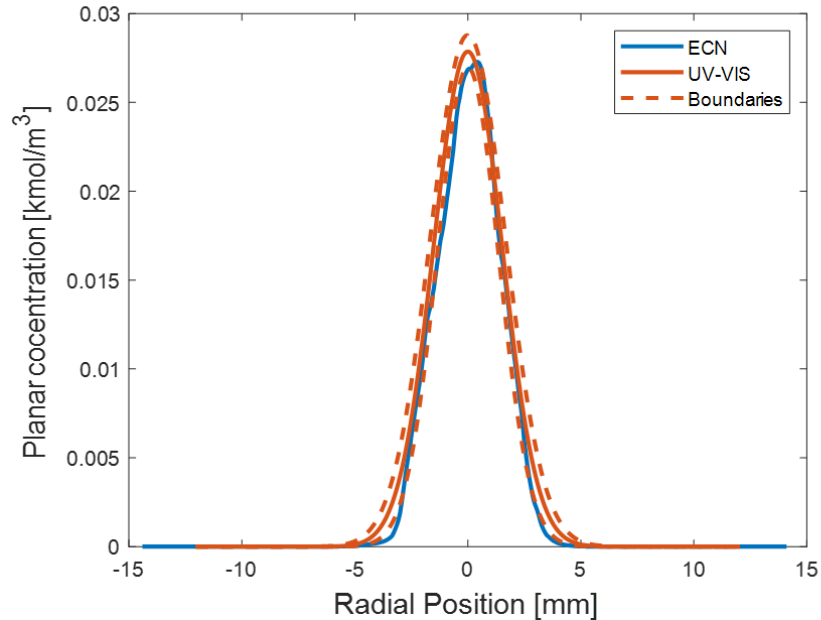


Figure 44. Planar fuel concentration comparison for a radial plot at 20 mm from the nozzle

In Figure 44 the difference between the mean UV-Vis DBI planar fuel concentration and its upper and lower uncertainty bounds is maximum at the center of the spray, while for the edges, this difference is lower. On the other hand, in Figure 45 the difference is higher on the edges than at the center of the spray.

However, both types of radial plots of the UV-VIS DBI data match well with the planar fuel concentration measurements obtained by Rayleigh scattering. Moreover, the uncertainty introduced by the inverse Abel transform is low compared to the mean.

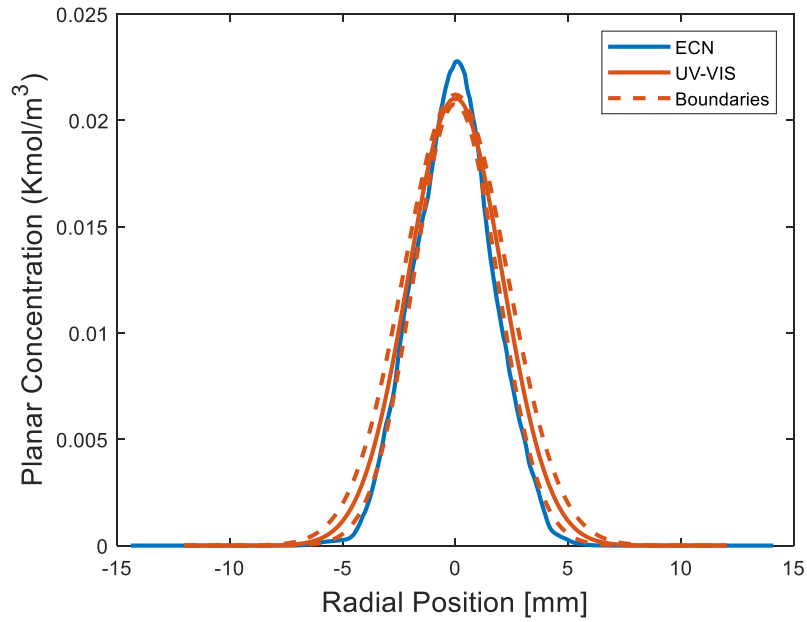


Figure 45. Planar fuel concentration comparison for a radial plot at 25 mm from the nozzle

Chapter 6. CONCLUSION

Through this project, we have identified two key challenges for quantifying air-fuel mixing measurements with the UV-Vis DBI technique. First, the high cost and time consuming of these mixing measurements limit the amount of the data that can be used. And second, the different nature of the data gathered by this line-of-sight technique requires validation with other quantitative measurements such as the Rayleigh scattering data.

Prior to performing any analysis, the data must be checked to detect any irregularities in the images acquired. In our case, we found two main problems that had to be corrected: the time misaligning of the individual injections, and the presence of outliers. Then through the use of the standard deviation and the confidence interval, we could identify that in order to determine a statistically relevant ensemble average, 30-40 injections were needed.

Afterwards, the inverse Abel transform was applied to our UV-Vis DBI data to evaluate it against the Rayleigh scattering data. It was observed that the transformed line-of-sight data matched well with the planar measurements provided by ECN.

In addition, we analyzed how the uncertainty of the mean propagated through the inverse Abel transform. It resulted that the uncertainty of the mean could be propagated principally as fluctuations in the centerline and the edges of the spray.

Finally, in order to achieve quantitative results using this technique, the pressure dependence of the absorption coefficient of naphthalene will be investigated in a future work of this research group.

Chapter 7. REFERENCES

- [1] I. E. Agency, «CO₂ emissions from fuel combustion,» 2019.
- [2] R. O'Driscoll, M. Stettler, N. Molden, T. Oxley y H. ApSimon, «Real world CO₂ and NO_x emissions from 149 Euro 5 and 6 diesel, gasoline and hybrid passenger cars,» *Science of the Total Environment*, vol. 621, pp. 282-290, 2018.
- [3] H. Ritchie and M. Roser, "CO₂ and Greenhouse Gas Emissions," *Our World in Data*, 2017.
- [4] J. Dec, «Advanced compression-ignition engines - Understanding the in-cylinder processes,» *Proceedings of the Combustion Institute*, vol. 32, n° 2, pp. 2727-2742, 2009.
- [5] N. Ramesh y J. M. Mallikarjuna, «Evaluation of in-cylinder mixture homogeneity in a diesel HCCI engine – A CFD analysis,» *Engineering Science and Technology, an International Journal*, vol. 19, n° 2, pp. 917-925, 2016.
- [6] C. A. Idicheria and L. M. Pickett, "Quantitative mixing measurements in a vaporizing diesel spray by rayleigh imaging," *SAE Technical Papers*, 2007.
- [7] A. S. Cheng, A. Upatnieks and C. J. Mueller, "Investigation of the impact of biodiesel fuelling on NO_x emissions using an optical direct injection diesel engine," *International Journal of Engine Research*, vol. 7, no. 4, pp. 297-318, 2006.

- [8] C. Mueller, A. Boehman y G. Martin, «Investigation of the origin of increased NO_x emissions in a heavy-duty compression-ignition engine fueled with soy biodiesel,» *ACS National Meeting Book of Abstracts*, vol. 2, nº 1, 2009.
- [9] L. M. Pickett and D. L. Siebers, "Soot in diesel fuel jets: effects of ambient temperature, ambient density, and injection pressure," *Combustion and Flame*, vol. 138, no. 1-2, pp. 114-135, 2004.
- [10] M. Suzuki, K. Nishida and H. Hiroyasu, "Simultaneous concentration measurement of vapor and liquid in an evaporating diesel spray," *SAE Technical Papers*, no. 412, 1993.
- [11] J. Egermann, A. Göttler y A. Leipertz, «Application of spontaneous Raman scattering for studying the diesel mixture formation process under near-wall conditions,» *SAE Technical Papers*, nº 724, 2001.
- [12] J. M. Desantes, J. V. Pastor, J. M. Pastor y J. E. Julia, «Limitations on the use of the planar laser induced exciplex fluorescence technique in diesel sprays,» *Fuel*, vol. 84, nº 18, pp. 2301-2315, 2005.
- [13] M. Kerker, «The Scattering of Light and Other Electro- magnetic Radiation,» *Academic Press*, 1969.
- [14] C. Bohren y D. Huffman, «Absorption and Scattering of Light by Small Particles,» 1983.
- [15] F. Robben, «Comparison of density and temperature measurement using raman scattering and Rayleigh scattering, in Combustion Measurements in Jet Propulsion Systems,» *Project SQUID Workshop Proceedings PU-RI-76*, 1975.

- [16] C. Espey, J. E. Dec, T. Litzinger y D. Santavicca, «Planar laser rayleigh scattering for quantitative vapor-fuel imaging in a diesel jet,» *Combustion and Flame*, vol. 109, nº 1-2, pp. 65-86, 1997.
- [17] L. M. Pickett, J. Manin, C. L. Genzale, M. Musculus, D. Siebers y I. Cherian A., «Relationship between diesel fuel spray vapor penetration/dispersion and local fuel mixture fraction,» *SAE International Journal of Engines*, vol. 4, nº 1, p. 764, 2011.
- [18] A. R. Chraplyvy, «Nonintrusive measurements of vapor concentrations inside sprays,» *IEEE Journal of Quantum Electronics*, vol. 17, nº 12, pp. 2620-2624, 1981.
- [19] J. Drallmeier y J. Peters, «Experimental Investigation of Fuel Spray Vapor Phase Characterization,» *Atomization and Sprays*, vol. 1, nº 63, 1991.
- [20] M. Adachi, V. McDonnell y G. Samuelsen, «Non-Intrusive Measurement of Gaseous Species in Reacting and Non-Reacting Sprays,» *Combustion Science and Technology*, vol. 75, pp. 179-194, 1991.
- [21] H. Zhao and N. Ladommatos, "Optical diagnostics for in-cylinder mixture formation measurements in IC engines," *Progress in Energy and Combustion Science*, vol. 24, no. 4, pp. 297-336, 1998.
- [22] A. Kastengren, C. Powell, Z. Liu y J. Wang, «Time Resolved , Three Dimensional Mass Distribution of Diesel Sprays Measured with X-Ray Radiography,» *Argonne National Laboratory*, 2009.
- [23] A. Kak y M. Slaney, «Principles of Computerized Tomographic Imaging,» *IEEE Press*, p. 186, 1988.

- [24] A. Kastengren, F. Z. Tilocco, D. Duke, C. F. Powell, S. Moon and X. Zhang, "Time-Resolved X-Ray Radiography of Sprays from Engine Combustion Network Spray A Diesel Injectors," *Atomization and Sprays*, vol. 24, no. 3, p. 251–272, 2014.
- [25] L. Weiss, M. Wensing, J. Hwang, L. Pickett y S. Skeen, «Development of limited-view tomography for measurement of Spray G plume direction and liquid volume fraction,» *Experiments in Fluids*, vol. 61, nº 2, pp. 1-17, 2020.
- [26] L. Pickett, S. Kook y M. Musculus, «Influence of Diesel Injection Parameters on End-of-Injection Liquid Length Recession,» *SAE Int. J. Engines*, vol. 2, nº 1, pp. 1194-1210, 2009.
- [27] N. H. Abel, «Auflösung einer mechanischen Aufgabe.,» *Journal für die reine und angewandte Mathematik*, pp. 153-157, 1826.
- [28] D. Hickstein, S. Gibson, R. Yurchak, D. Das and M. Ryazanov, "A direct comparison of high-speed methods for the numerical Abel transform," *Review of Scientific Instruments* 90, 2019.
- [29] C. J. Dash, «One-dimensional tomography: a comparison of Abel, onion-peeling, and filtered backprojection methods,» *Applied Optics*, vol. 31, nº 8, 1992.
- [30] " ECN (Engine Combustion Network)," [Online]. Available: <https://ecn.sandia.gov/>.
- [31] J. Johnson, B. Somers y M. Meirjer, «Characterization and comparison of boundary conditions for different combustion vessels,» 2012.
- [32] C. Godbold, F. Poursadegh, O. Bibik, C. de la Camara Castillo y C. Genzale, «A multi-wavelength extinction imaging diagnostic for quantifying diesel spray mixing at engine-relevant conditions,» *ASME*, 2020.

- [33] B. Knox, «End-of-Injection Effects on Diesel Spray Combustion,» *phD Thesis*, 2016.
- [34] H. Grosch, Z. Sárossy, H. Egsgaard and A. Fateev, "UV absorption cross-sections of phenol and naphthalene at temperatures up to 500°C," *Journal of Quantitative Spectroscopy and Radiative Transfer*, vol. 156, pp. 17-23, 2015.
- [35] M. Orain, P. Baranger, B. Rossow y F. Grisch, «Fluorescence spectroscopy of naphthalene at high temperatures and pressures: Implications for fuel-concentration measurements,» *Applied Physics B*, vol. 102, pp. 163-172, 2011.
- [36] E. Instruments, «The Beer-Lambert Law,» [En línea]. Available: <https://www.edinst.com/blog/the-beer-lambert-law/>.
- [37] M. Firman, «MATLAB Central File Exchange,» 2016. [En línea]. Available: <https://www.mathworks.com/matlabcentral/fileexchange/60271-2d-abel-inversion>.
- [38] M. Kasim, «Quantitative single shot and spatially resolved plasma wakefield diagnostics,» *Phys. Rev. Spec. Top. - Accel. Beams*, vol. 18, n° 8, 2015.
- [39] R. Bracewell, «The Fourier Transform and Its Applications, 3rd ed,» *McGraw-Hill*, pp. 262-266, 1999.
- [40] ECN, «Rayleigh scattering n-dodecane/ambient mixing images for Spray A and several other experimental conditions,» [En línea]. Available: <https://ecn.sandia.gov/data/bklDaal4mixing/>.
- [41] H. Abdi y P. Molin, «Lilliefors/Van Soest's test of normality,» *Encyclopedia of Measurement and Statistics.*, 2007.

APPENDIX I. SUSTAINABLE DEVELOPMENT GOALS

This project contributes to the development of a new imaging technique for mixing measurements experiment. This new diagnosis setup will allow much near nozzle measurements of the spray concentration. A deeper understanding of the air-fuel mixing problem can definitively help to improve the efficiency of the combustion leading to fewer emissions and lower consumption, this could have different positive effects on sustainable development.

- Target 7. Lowering the emissions and improving the energy efficiency of the diesel engines clearly aligns with target 7 about affordable and clean energy of the sustainable development goals. More specifically, it aligns with target 7.3 “By 2030, double the global rate of improvement in energy efficiency” and 7.A “By 2030, enhance international cooperation to facilitate access to clean energy research and technology, including renewable energy, energy efficiency and advanced and cleaner fossil-fuel technology, and promote investment in energy infrastructure and clean energy technology”. Both targets are supported by the better efficiency of the combustion that leads to a lower fuel consumption, which means that there is a better usage of the diesel.
- Target 9. This target is about industries, innovation, and infrastructure. The research developed in this document contributes to the innovation of a new imaging technique. This innovation can provide an improved testing vessel for diesel engines. As a result,

the automation industry will benefit from the improvements and findings of this imaging technique. Target 9.5 describes the contribution described above: “Enhance scientific research, upgrade the technological capabilities of industrial sectors in all countries, in particular developing countries, including, by 2030, encouraging innovation and substantially increasing the number of research and development workers per 1 million people and public and private research and development spending”.

- Target 11. Improving the efficiency and the emissions of diesel engines can help with target 11 about making cities more inclusive, resilient, sustainable and safer. The impact of this research group can, in a future, make diesel engines more affordable and sustainable. As a result, the access to affordable and sustainable transportation can be expanded, which aligns with target 11.2 “By 2030, provide access to safe, affordable, accessible and sustainable transport systems for all, improving road safety, notably by expanding public transport, with special attention to the needs of those in vulnerable situations, women, children, persons with disabilities and older persons”.